Electronic Supplementary Material (ESI) for Journal of Materials Chemistry A.

Supporting Information for:

Mixed metal-antimony oxide nanocomposites: low pH water oxidation electrocatalysts with outstanding durability at ambient and elevated temperatures

Sibimol Luke,[a,b,c] Manjunath Chatti,[d,‡] Asha Yadav,[e,‡] Brittany V. Kerr,[f] Jiban Kangsabanik,[e] Tim Williams,[g] Pavel V. Cherepanov,[d] Bernt Johannessen,[h] Akshat Tanksale,[c] Douglas R. MacFarlane,[d,i] Rosalie K. Hocking,[f,*] Aftab Alam,[e,*] Aswani Yella,[b,*] Alexandr N. Simonov,[d,i,*]

[a] IITB-Monash Research Academy, IIT Bombay, Mumbai 400076, India

[b] Department of Metallurgical Engineering and Materials Science, IIT Bombay, Powai, Mumbai 400076, India. E-mail: aswani.yella@iitb.ac.in.

[c] Department of Chemical Engineering, Monash University, Victoria 3800, Australia

[d] School of Chemistry, Monash University, Victoria 3800, Australia.
E-mail: alexandr.simonov@monash.edu.

[e] Department of Physics, IIT Bombay, Powai, Mumbai 400076, India. E-mail: aftab@phy.iitb.ac.in

[f] Department of Chemistry and Biotechnology, Swinburne University of Technology, Hawthorn, Victoria 3122, Australia. E-mail: rhocking@swin.edu.au

[g] Monash Centre for Electron Microscopy, Victoria 3800, Australia

[h] Australian Synchrotron, Clayton, Victoria 3168, Australia

TABLE OF CONTENTS

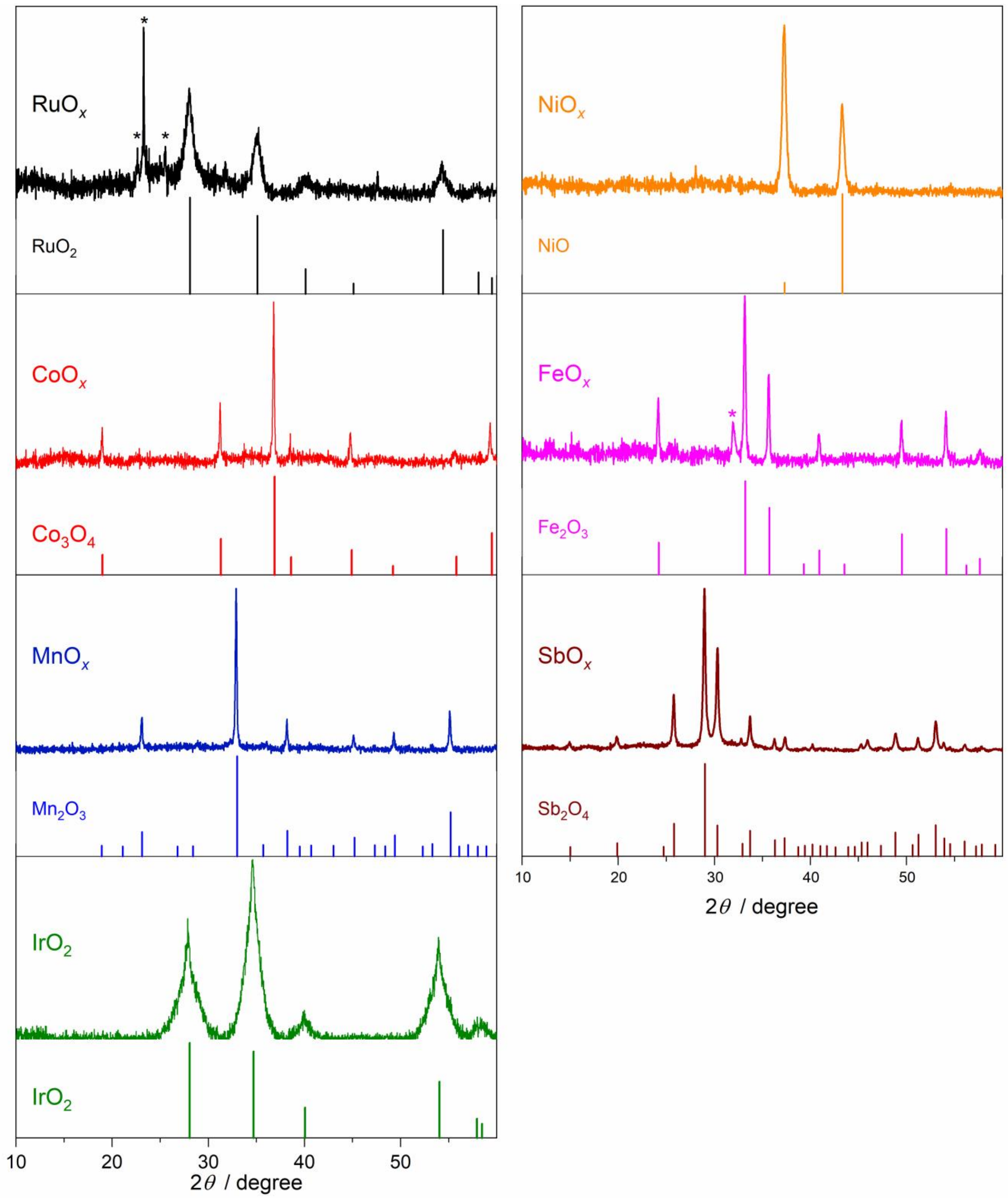

Figure S1. X-ray diffractograms for individual oxides investigated herein along with the tabulated positions and intensities of reflections for RuO_2 (ICSD – 84619), Co_3O_4 (ICSD – 36256), Mn_2O_3 (ICSD – 9090), IrO_2 (ICSD-00-015-0870), NiO (ICSD – 28910), Fe_2O_3 (ICSD – 40142), and Sb_2O_4 (ICSD – 153154). Mean crystallite sizes calculated using the Scherrer equation were *ca* 18 nm for RuO_2, *ca* 48 nm for Co_3O_4, *ca* 45 nm for Mn_2O_3, *ca* 8 nm for IrO_2, *ca* 16 nm for NiO, *ca* 34 nm for Fe_2O_3, and *ca* 30 nm for Sb_2O_4. Peaks marked with * might be attributed to (a) RuO_4 (ICSD – 98-009-4978) and (b) Fe_3O_4 (ICSD – 96-900-2027).

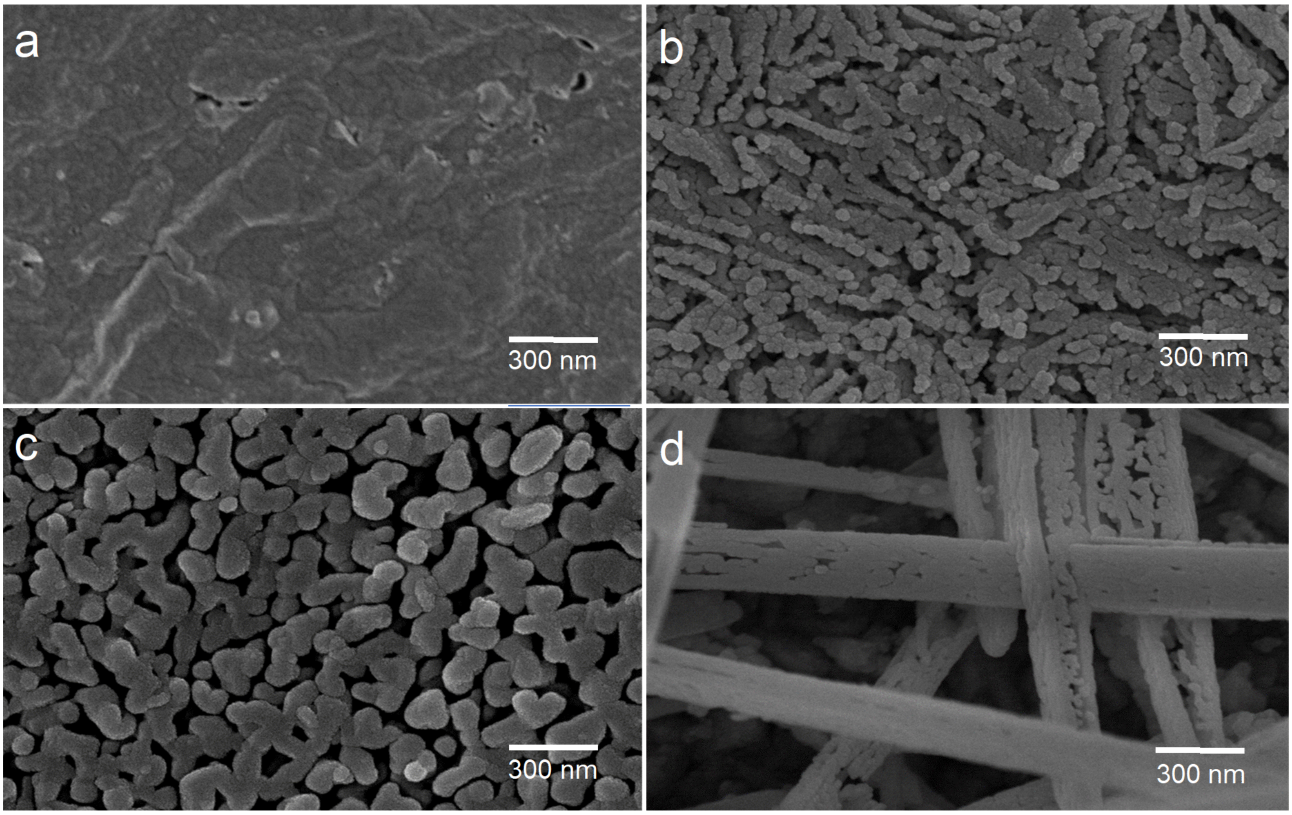

Figure S2. Scanning electron micrographs of (a) RuO_x, (b) CoO_x, (c) MnO_x and (d) SbO_x.

ELECTROCATALYTIC ACTIVITY OF INDIVIDUAL OXIDES

Under voltammetric conditions, all as-prepared monometallic oxides exhibited measurable catalytic activity towards water electrooxidation in contrast to SbO_x, which produced negligible oxidation currents up to 2.2 V *vs.* reversible hydrogen electrode (RHE) (Figures S3). Notwithstanding its reasonable initial activity, RuO_x was highly unstable in 0.5 M H_2SO_4 (Figures S3e and S4a), consistent with previous reports.[S1] Upon initial loss of activity during the first hour of tests at a current density of 10 mA cm^{-2} (hereinafter, all currents are normalised to the geometric surface area of the electrodes), RuO_x was further able to sustain this rate of the OER at an IR_u-corrected potential (E_{IR}) of *ca* 2.0 V *vs.* RHE for more than 23 h (Figure S4a), although subsequent short-term potentiostatic tests revealed that the performance was still slowly degrading (Figure S4c). Degradation of RuO_x might be interpreted in terms of the formation of soluble hyperruthenic acid,[S2, S3] while the remaining catalytic activity might be attributed to the oxides of ruthenium in higher oxidation states that remain quasi-stable on the electrode surface yet are not highly catalytically active for the OER under the employed conditions.[S4]

Among the examined non-noble metal oxides, CoO_x exhibited the best initial electrocatalytic activity enabling the rate of the OER of 10 mA cm^{-2} at an IR_u-corrected overpotential (η_{IR}) of only *ca* 0.53 V (Figure S4a), which is comparable to the results reported by Schaak and colleagues ($\eta_{IR} \approx 0.58$ V).[S5] Cobalt oxide synthesised herein sustained its initial activity for *ca* 5 h (*cf.* 12 h in Ref.[S5]) before visually complete dissolution and dramatic deterioration of the activity occurred, as expected from the Pourbaix diagram.[S6] Nevertheless, the quasi-stabilised performance was still better than that of blank FTO suggesting that a very small amount of catalytic CoO_x still remained on the surface (Figure S4a), probably, operating through a self-healing mechanism.[S7] However, the CoO_x remaining on the electrode could not be detected by cyclic voltammetry (Figure S5a), either reflecting their low amount or instability at not very positive potentials.[S7, S8] FeO_x exhibited qualitatively similar behaviour to that of CoO_x, although the initial activity was worse, and the final performance was close to that of unmodified FTO; NiO_x suffered essentially immediate dissolution (Figure S3c and S4b).

Manganese and antimony oxides demonstrated low activity towards the OER, but their performance was stable and even slightly improved during tests under ambient conditions on a 24 h timescale (Figure S4a and S4b). This was accompanied by essentially complete loss of the voltammetric signals associated with the Mn redox transformations, again pointing to a possibility for the catalytically active MnO_x being formed on the electrode surface at positive potentials only (Figure S5b). In the SbO_x case, a notable enhancement of the featureless pseudocapacitive currents, most likely reflecting the roughening of the material surface resulting in the minor activity improvement, was observed (Figure S5f). The quasi-stabilised overpotential required to maintain the OER rate of 10 mA cm^{-2} with SbO_x- and MnO_x-functionalised electrodes was *ca* 1.15 and 0.84, respectively (Figure S4).

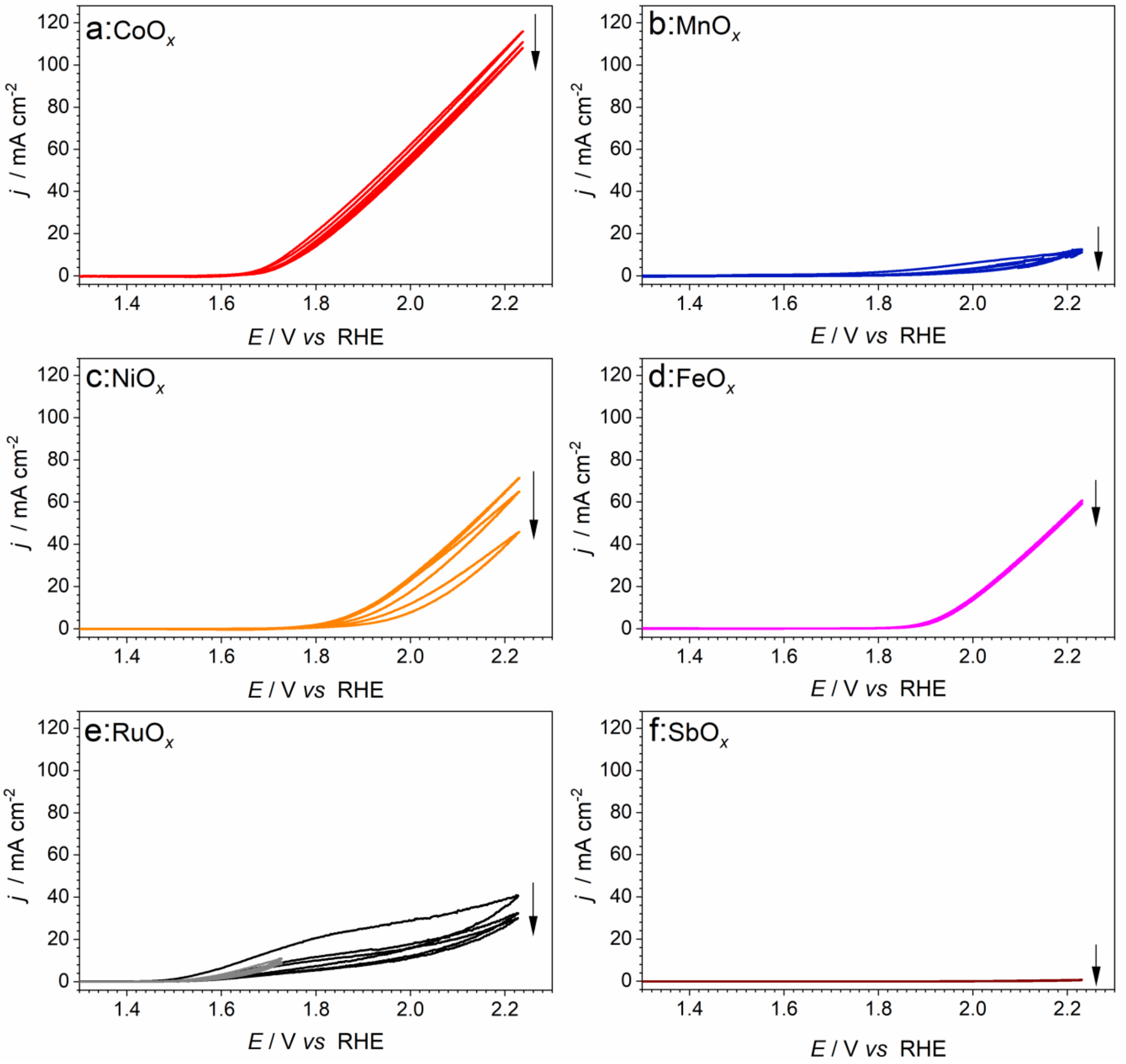

Figure S3. Cyclic voltammetry (scan rate, $\nu = 0.020$ V s^{-1}; potentials are not IR_u-corrected) recorded at ambient temperature using stirred 0.5 M H_2SO_4 electrolyte solution and FTO electrodes modified with as-prepared metal oxides: (a) CoO_x, (b) MnO_x, (c) NiO_x, (d) FeO_x, (e) RuO_x, and (f) SbO_x. For RuO_x, voltammograms recorded up to 1.73 (*grey*) and 2.23 V *vs.* RHE (*black*) are shown. Currents are normalised to the geometric surface area. Arrows show the evolution of the voltammetric response with cycling.

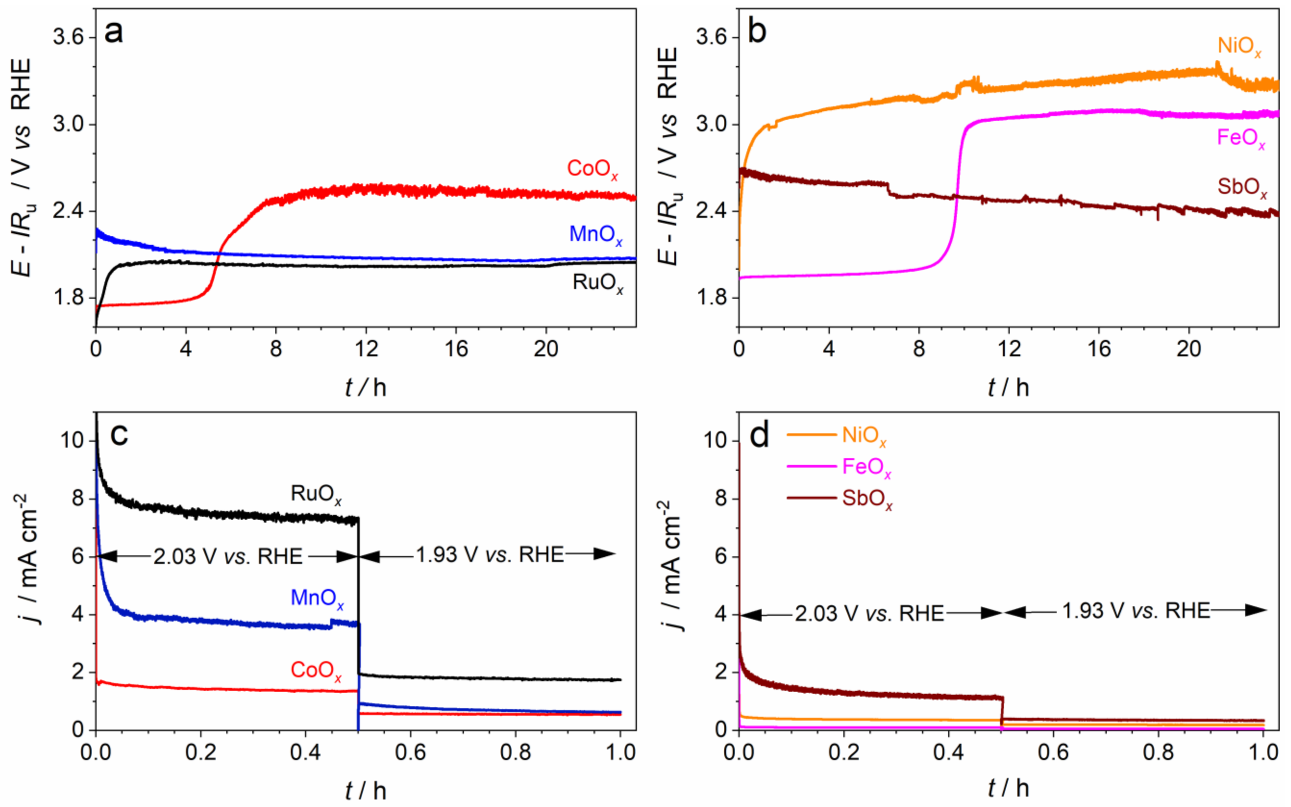

Figure S4. (a-b) Chronopotentiograms at 10 mA $cm^{-2}{}_{geom.}$ corrected for ohmic losses, and (c-d) chronoamperograms at non-corrected potentials of 2.03 and 1.93 V *vs.* RHE recorded for FTO electrodes functionalised with RuO_x (*black*), CoO_x (*red*), MnO_x (*blue*), NiO_x (*orange*), FeO_x (*magenta*), and SbO_x (*brown*) in contact with 0.5 M H_2SO_4 at 24 ± 2 °C. Data in panels (c) and (d) were obtained immediately after measurements shown in panels (a) and (b), respectively. Currents are normalised to the geometric surface area.

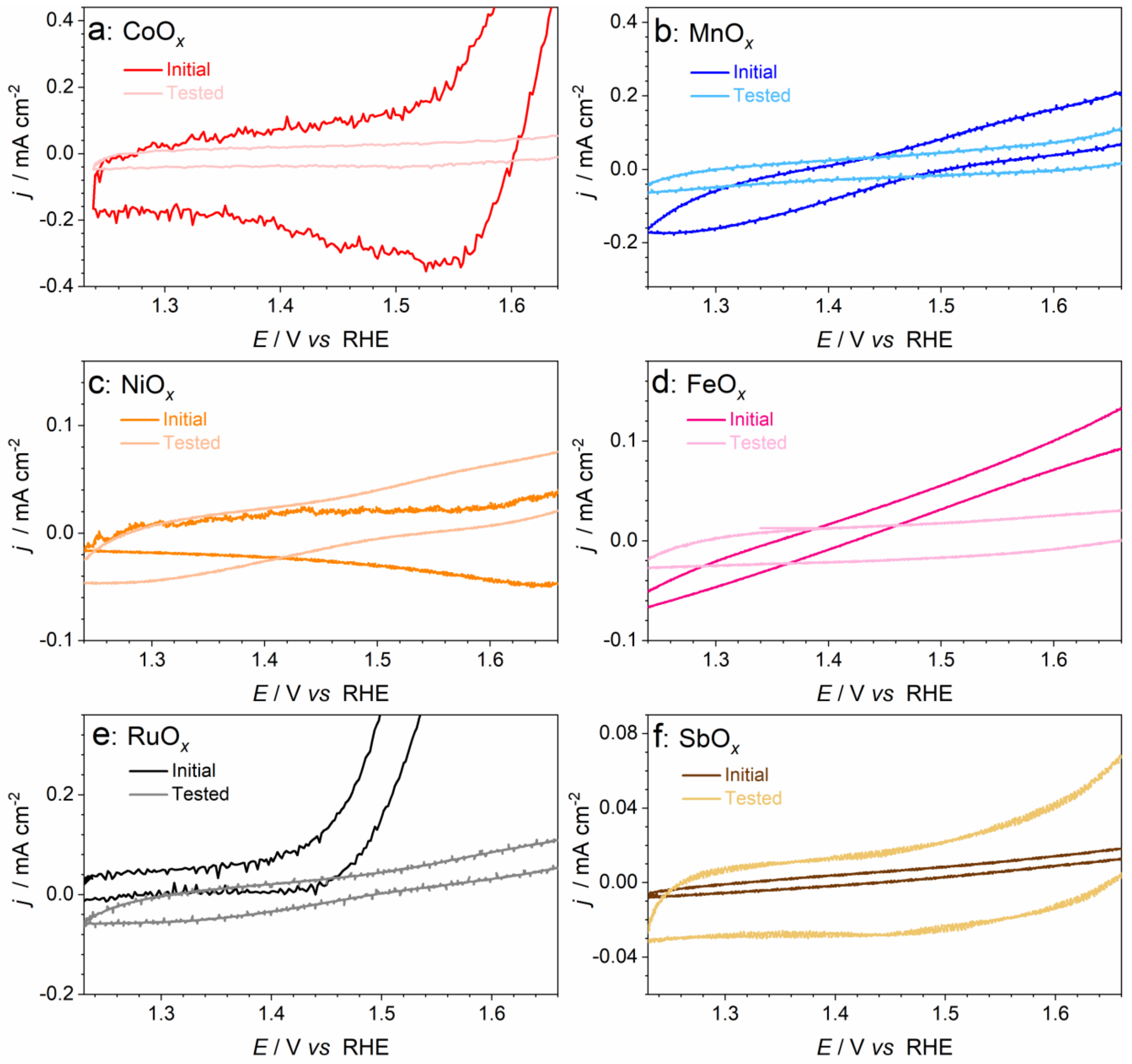

Figure S5. Comparison of the pre-catalytic regions of the quasi-stabilised cyclic voltammograms (scan rate, v = 0.020 V s^{-1}) of (a) CoO$_x$, (b) MnO$_x$, (c) NiO$_x$, (d) FeO$_x$ (e) RuO$_x$ and (f) SbO$_x$ in 0.5 M H_2SO_4 at ambient temperature before (pale traces) and after (vivid traces) 25 h durability tests (24 h at 10 mA cm^{-2}; 0.5 h at 2.03 V *vs.* RHE; 0.5 h at 1.93 V *vs.* RHE) under the same conditions. Currents are normalised to the geometric surface area of the electrode; potentials were not corrected for the IR_u-drop.

Table S1. Loss of metals and antimony from catalysts (at.%)[a] during the OER in 0.5 M H_2SO_4.[b]

Catalyst	Exp.	Time / h	24 ± 2 °C		Time / h	80 ± 1 °C	
			Metal	Sb		Metal	Sb
[Mn+Sb]O$_y$	1	25	21 *1.1×10^{4}*	17 *1.4×10^{4}*		Not analysed	
	2	0.16	5.8 *2.7×10^{2}*	3.5 *4.4×10^{2}*		Not analysed	
		4	10 *8.3×10^{3}*	12 *4.2×10^{3}*			
		8	12 *1.7×10^{4}*	15 *1.5×10^{4}*			
		12	14 *1.9×10^{4}*	17 *1.4×10^{4}*			
		20	17 *2.8×10^{4}*	21 *2.0×10^{4}*			
		24	18 *2.4×10^{4}*	23 *1.9×10^{4}*			
		28	19 *5.7×10^{4}*	24 *2.6×10^{4}*			
[Co+Sb]O$_y$	1	25	15 *1.5×10^{4}*	26 *8.7×10^{3}*		Not analysed	
[Ru+Sb]O$_y$	1	25	1 *2.3×10^{5}*	37 *7.7×10^{3}*	193	3 *6.4×10^{5}*	47 *4.0×10^{4}*
	2	0.16	0.63 *2.5×10^{3}*	4.9 *3.2×10^{2}*	0.16	3.7 *4.2×10^{2}*	12 *1.3×10^{2}*
		4	1.2 *6.5×10^{4}*	9.4 *7.9×10^{3}*	4	4.0 *9.5×10^{4}*	34 *1.6×10^{3}*
		8	1.7 *7.5×10^{4}*	11 *1.7×10^{4}*	8	4.3 *2.4×10^{5}*	38 *1.0×10^{4}*
		12	1.8 *4.7×10^{5}*	14 *1.6×10^{4}*	12	5.3 *3.6×10^{4}*	38 *8.4×10^{4}*
		20	1.9 *4.2×10^{5}*	18 *1.8×10^{4}*	20	5.6 *2.2×10^{5}*	36 *∞*
		24	2.6 *5.9×10^{4}*	20 *2.3×10^{4}*	24	6.0 *9.4×10^{4}*	36 *4.5×10^{5}*
		28	3.0 *9.0×10^{4}*	21 *4.2×10^{4}*	28	6.3 *1.5×10^{5}*	36 *1.2×10^{5}*

[a] Calculation based on the amount of metal and Sb deposited onto electrodes (1 µmol cm^{-2} each) and the amounts measured in solutions after the OER tests by ICP-OES; values in italics are the corresponding S-numbers. [b] After initial EIS and voltammetric characterisation, the experiment was undertaken as follows: (1) galvanostatic test at 10 mA cm^{-2} for either 24 (at 24 ± 2 °C) or 192 h (at 80 ± 2 °C) followed by chronopotentiometry at 1.93 and 2.03 V *vs.* RHE for 0.5 h at each potential; (2) continuous galvanostatic test at 10 mA cm^{-2} with periodic sampling of the working electrolyte solution (5 mL of 20 mL) and replacement of the aliquot with 5 mL of pure 0.5 M H_2SO_4. Electrolyte solutions were continuously stirred during the chronoamperometric and chronopotentiometric measurements.

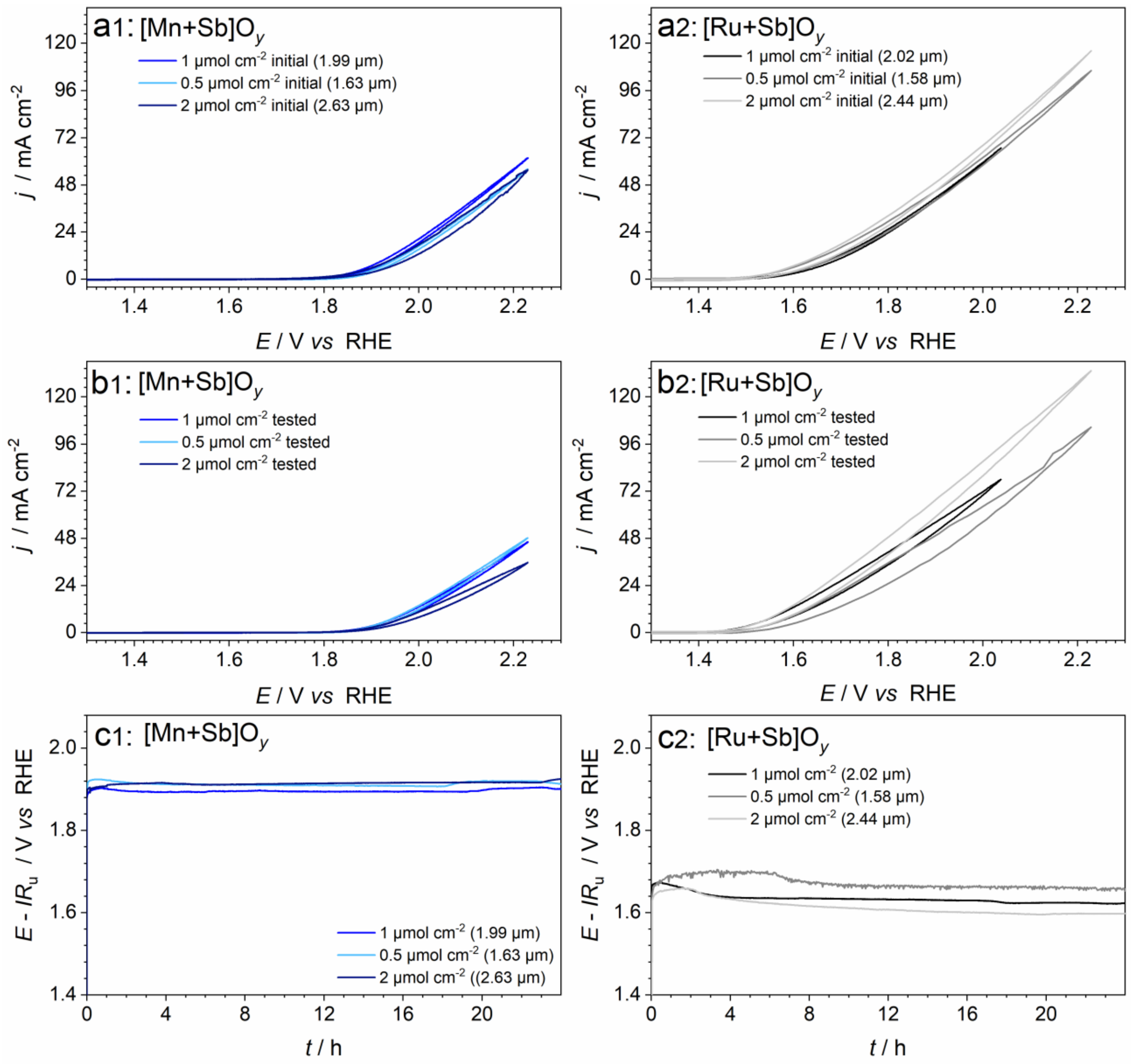

Figure S6. Electrocatalytic performance of the FTO electrodes modified with (1) [Mn+Sb]O$_y$ and (2) [Ru+Sb]O$_y$ at different loadings for the OER in stirred 0.5 M H_2SO_4 at 24 ± 2 °C: (a) initial and (b) final cyclic voltammetry (ν = 0.020 V s^{-1}; no IR_u-correction applied); (c) IR_u-corrected chronopotentiograms (10 mA cm^{-2}) recorded between voltammetric measurements shown in panels (a) and (b). The initial amount of metals and antimony deposited (only one value is shown since the initial M : Sb ratio was 1 : 1) along with thickness of the catalyst layers (in brackets) are shown in the figure legend. Apparent increase in the final (but not initial) activity of [Ru+Sb]O$_y$ with loading likely reflects slight roughening of the electrode surface during operation due to the loss of antimony oxide (Table S1; Figure S6). However, the differences between electrode with different loading are not significant and are incomparably lower than differences in the catalyst loading.

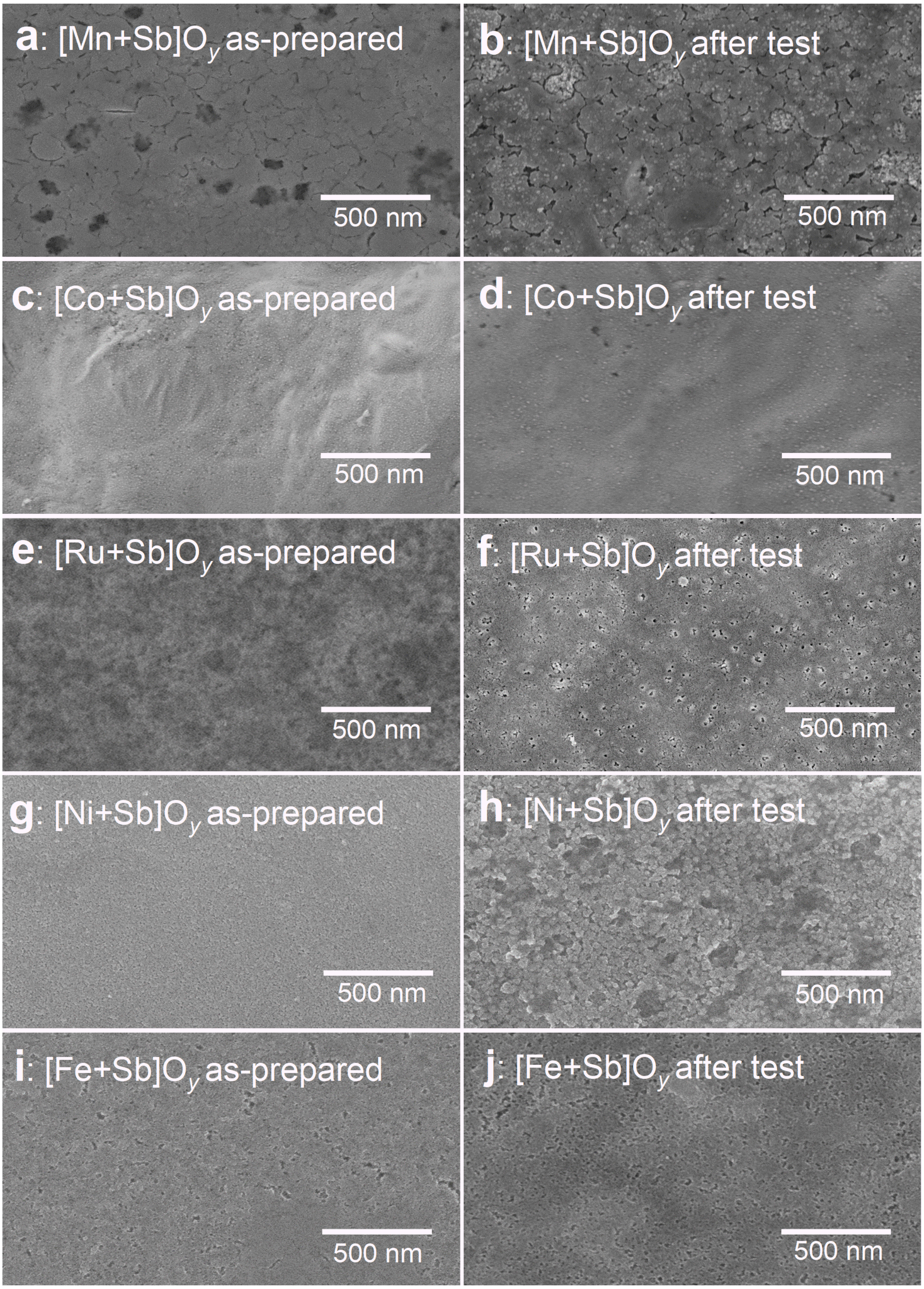

Figure S7. Scanning electron micrographs of (a-b) [Mn+Sb]O*y*, (c-d) [Co+Sb]O*y*, (e-f) [Ru+Sb]O*y*, (g, h) [Ni+Sb]O*y* and (i-j) [Fe+Sb]O*y* (a, c, e, g, i) before and (b, d, f, h, j) after 24 h galvanostatic (10 mA cm^{-2}) and subsequent 1 h potentiostatic (2.03 and 1.93 V *vs.* RHE for 0.5 h at each potential) operation in stirred 0.5 M H_2SO_4 at ambient temperature.

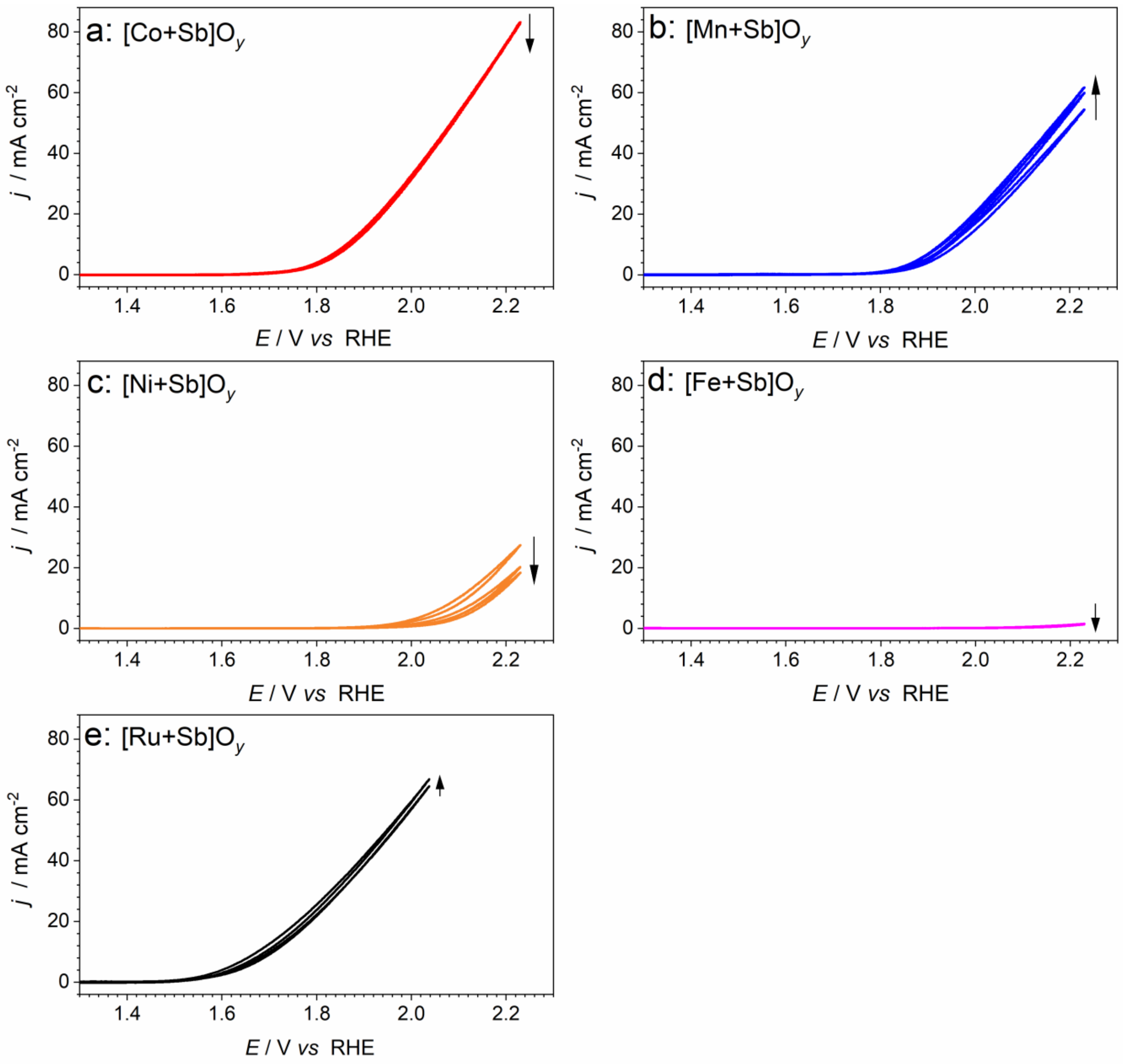

Figure S8. Evolution of cyclic voltammograms ($\nu = 0.020$ V s^{-1}; three consecutive cycles shown) of (a) [Co+Sb]O$_y$, (b) [Mn+Sb]O$_y$, (c) [Ni+Sb]O$_y$, (d) [Fe+Sb]O$_y$, and (e) [Ru+Sb]O$_y$ in 0.5 M H_2SO_4 at ambient temperature. Arrows show the evolution of the current density with cycling, while insets show magnified plots of the pre-catalytic regions. Currents are normalised to the geometric surface area of the electrode; potential values were not corrected for the IR_u-drop.

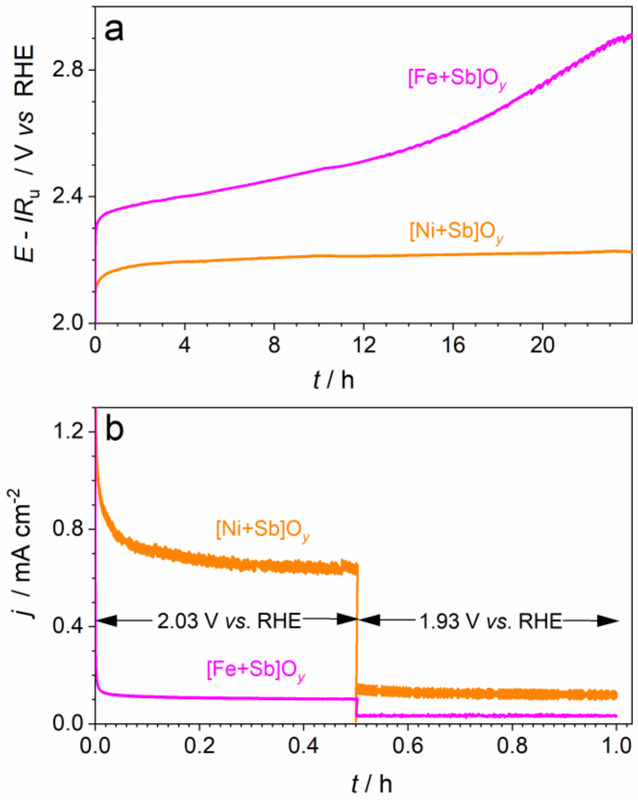

Figure S9. (a) Chronopotentiograms (current density 10 mA $cm^{-2}{}_{geom.}$) corrected for ohmic losses, and (b) chronoamperograms at non−IR_u corrected potentials of 2.03 and 1.93 V *vs.* RHE recorded for FTO electrodes modified with $[Ni+Sb]O_y$ (*orange*) and $[Fe+Sb]O_y$ (*magenta*) in contact with 0.5 M H_2SO_4 at 24 ± 2 °C. Chronoamperograms were recorded immediately after galvanostatic tests shown in panel (a). Currents are normalised to the geometric surface area.

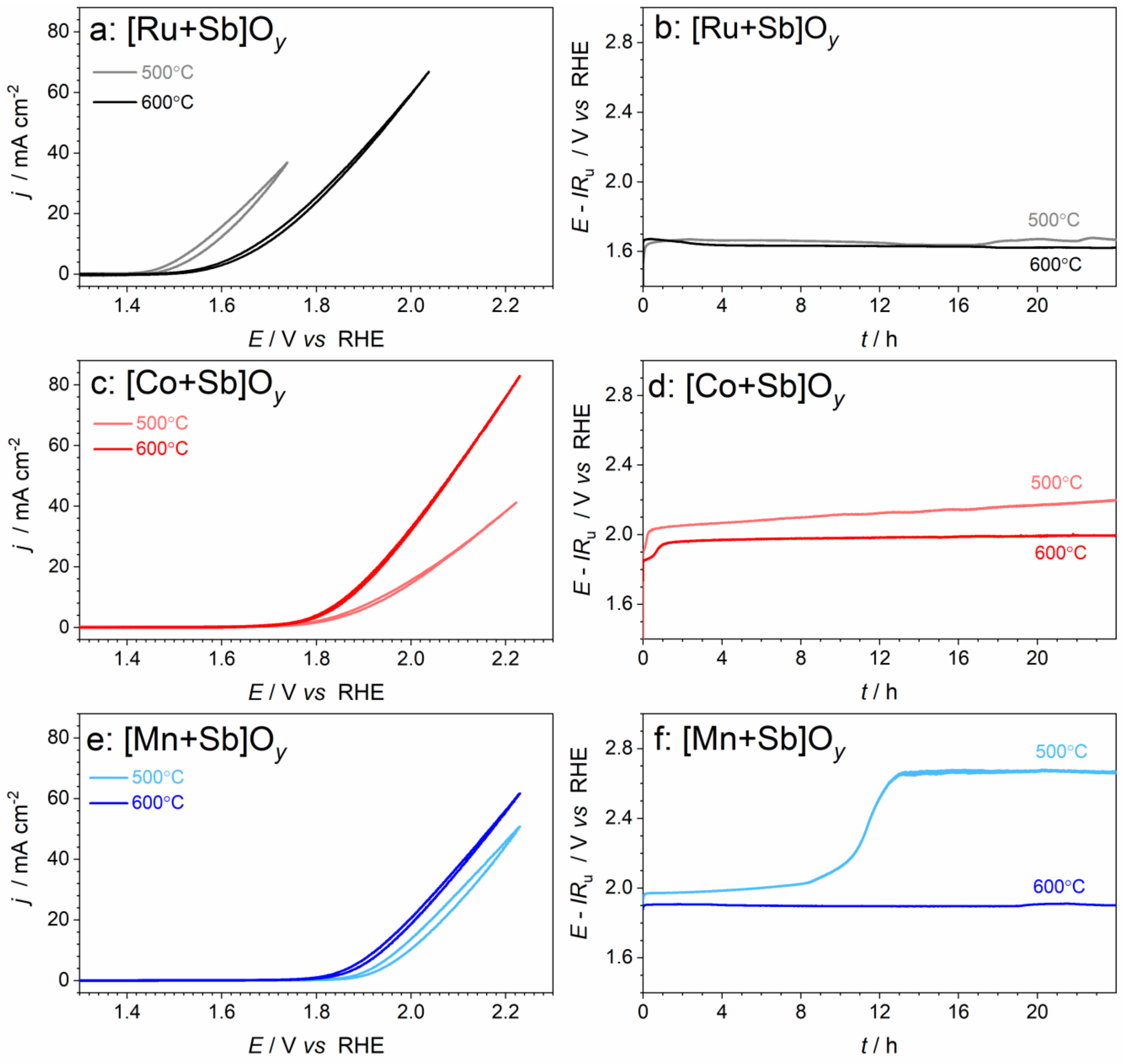

Figure S10. Effect of annealing temperature (500 °C – pale traces; 600 °C – vivid traces) on the electrocatalytic activity of (a-b) [Ru+Sb]O*y*, (c-d) [Co+Sb]O*y* and (e-f) [Mn+Sb]O*y* for the OER in 0.5 M H_2SO_4 at 24 ± 2 °C: (a, c, e) cyclic voltammetry (ν = 0.020 V s^{-1}; potentials are not IR_u-corrected), and (b, d, f) IR_u-corrected chronopotentiograms (current density 10 mA $cm^{-2}_{geom.}$).

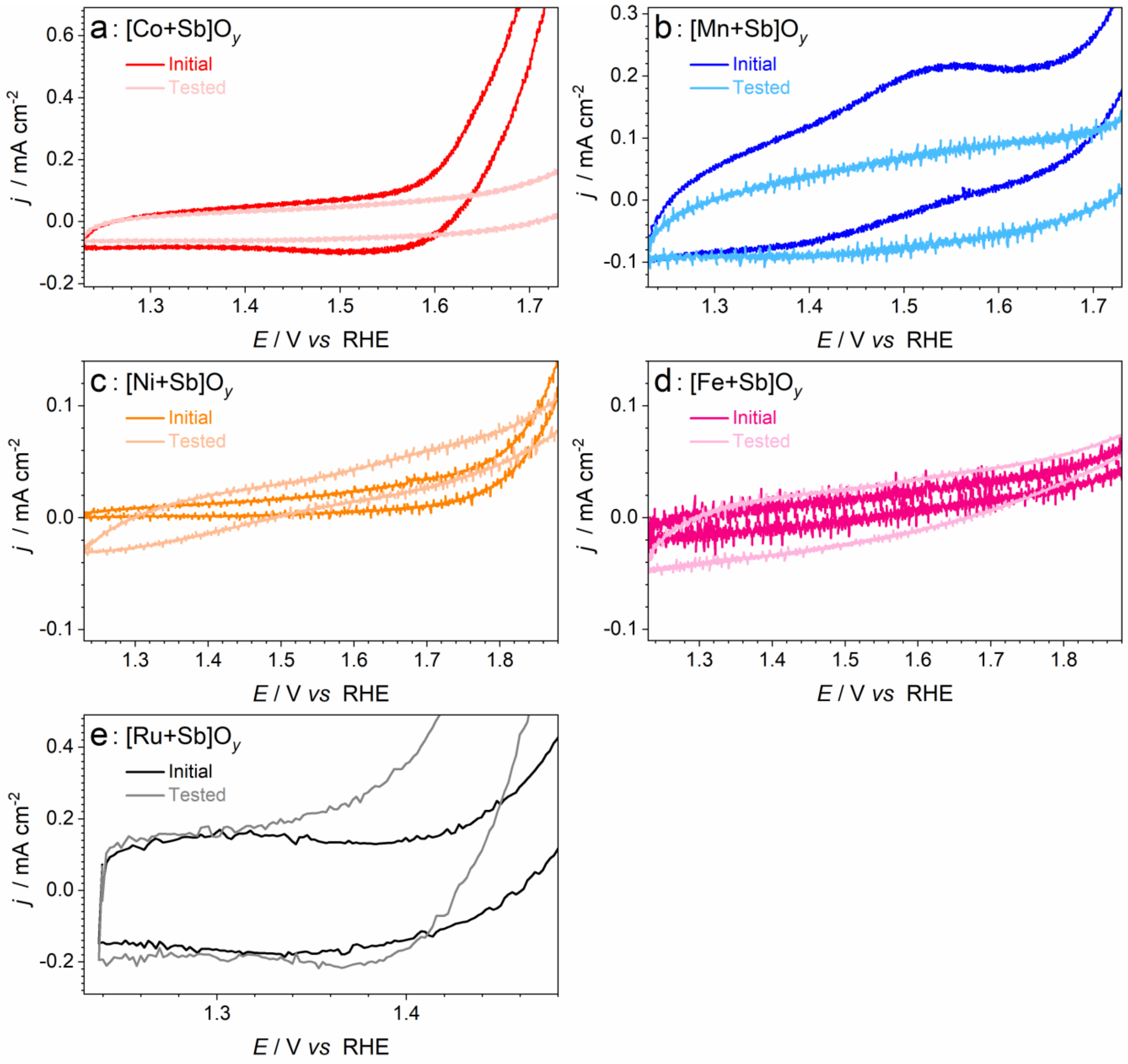

Figure S11. Comparison of the pre-catalytic regions of the quasi-stabilised cyclic voltammograms (ν = 0.020 V s^{-1}) of (a) [Co+Sb]O_y, (b) [Mn+Sb]O_y, (c) [Ni+Sb]O_y, (d) [Fe+Sb]O_y and (e) [Ru+Sb]O_y in 0.5 M H_2SO_4 at ambient temperature before (pale traces) and after (vivid traces) 25 h durability tests (24 h at 10 mA cm^{-2}; 0.5 h at 2.03 V *vs.* RHE; 0.5 h at 1.93 V *vs.* RHE) under the same conditions. Currents are normalised to the geometric surface area of the electrode; potentials were not corrected for the IR_u-drop.

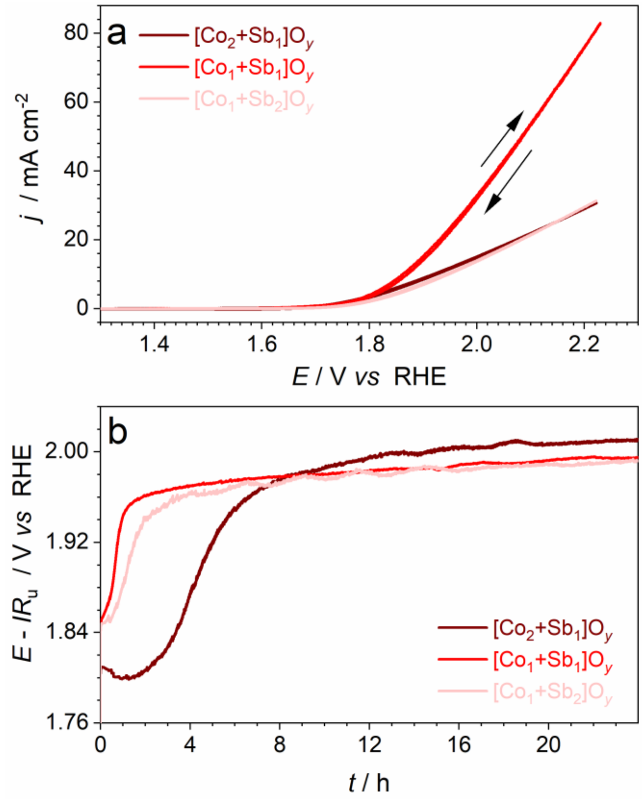

Figure S12. (a) Cyclic voltammetry (ν = 0.020 V s^{-1}; potentials are not corrected for the IR_u-drop), and (b) IR_u-corrected chronopotentiograms (current density 10 mA $cm^{-2}_{geom.}$) for FTO electrodes modified with cobalt-antimony oxides synthesised using different molar Co : Sb precursor ratios in contact with 0.5 M H_2SO_4 at 24 ± 2 °C. Currents are normalised to the geometric surface area. In panel (a), arrows exemplify the direction of the forward and backward sweeps.

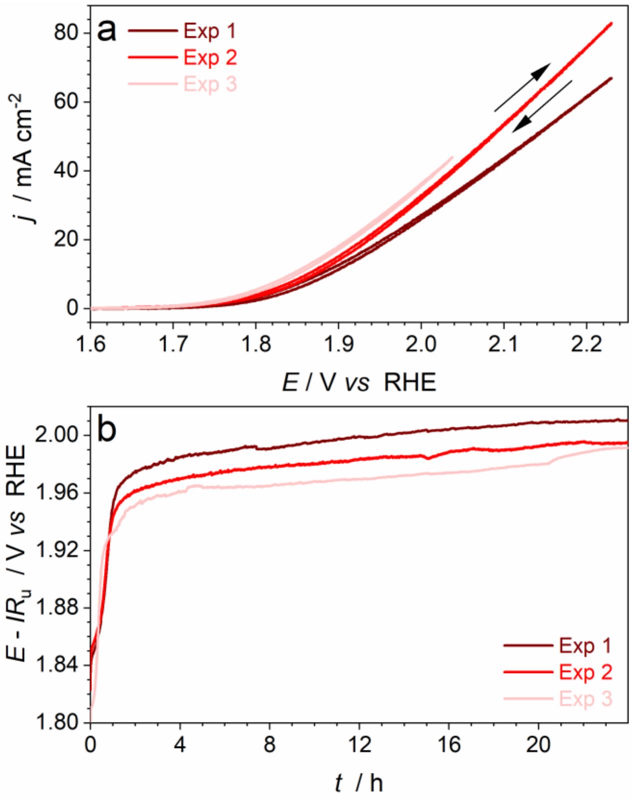

Figure S13. Reproducibility of the electrocatalytic properties of [Co+Sb]O_y (molar Co : Sb precursor ratio 1 : 1) demonstrated for three independent samples tested in 0.5 M H_2SO_4 at 24 ± 2 °C: (a) cyclic voltammetry (v = 0.020 V s^{-1}; potentials are not corrected for ohmic losses), and (b) IR_u-corrected chronopotentiograms (current density 10 mA $cm^{-2}_{geom.}$). Currents are normalised to the geometric surface area. In panel (a), arrows exemplify the direction of the forward and backward sweeps.

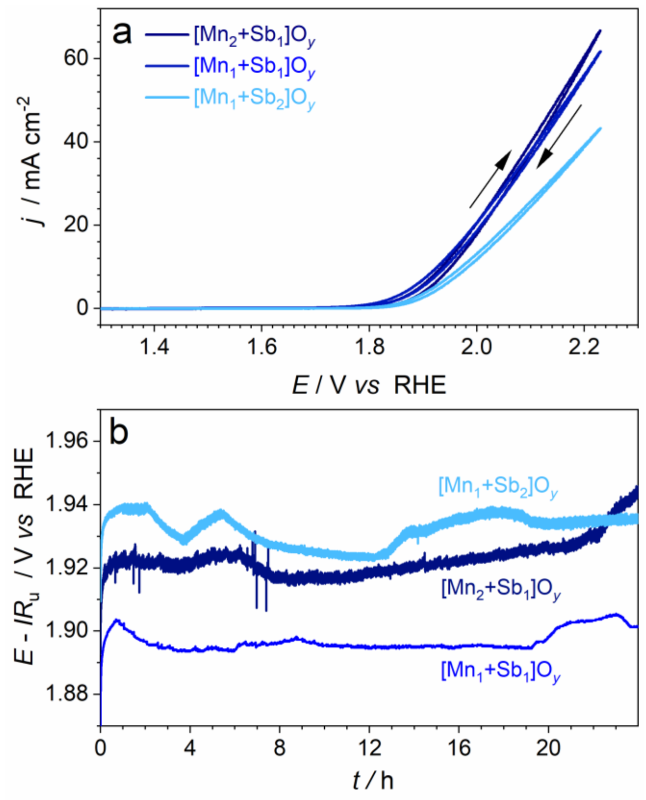

Figure S14. (a) Cyclic voltammetry (ν = 0.020 V s^{-1}; potentials are not corrected for the IR_u-drop), and (b) IR_u-corrected chronopotentiograms (current density 10 mA cm$^{-2}_{\text{geom.}}$) for FTO electrodes modified with manganese antimony oxides synthesised using different molar Mn : Sb precursor ratios in contact with 0.5 M H_2SO_4 at 24 ± 2 °C. Currents are normalised to the geometric surface area. In panel (a), arrows exemplify the direction of the forward and backward sweeps.

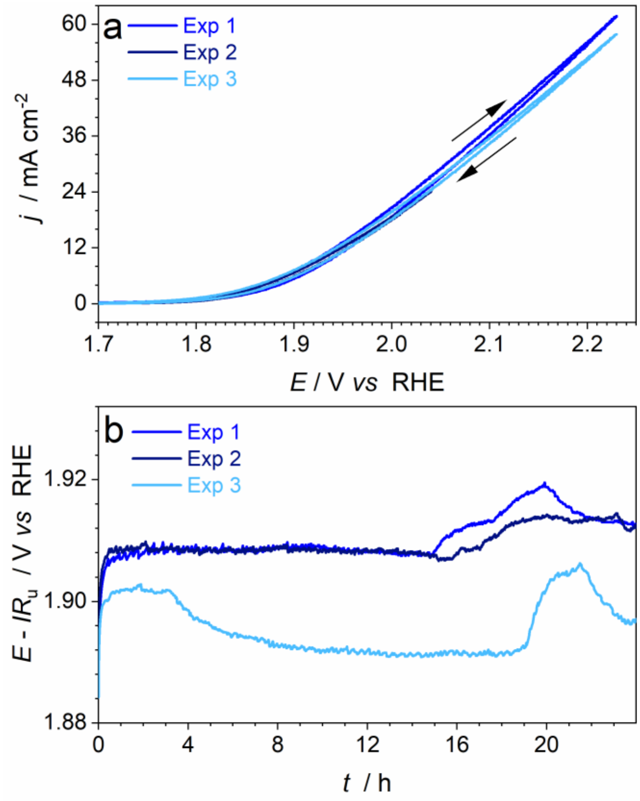

Figure S15. Reproducibility of the electrocatalytic properties of [Mn+Sb]O$_y$ demonstrated for three independent samples tested in 0.5 M H_2SO_4 at 24 ± 2 °C: (a) cyclic voltammetry (ν = 0.020 V s^{-1}; potentials are not corrected for ohmic losses), and (b) IR_u-corrected chronopotentiograms (current density 10 mA cm$^{-2}_{\mathrm{geom.}}$). Currents are normalised to the geometric surface area. In panel (a), arrows exemplify the direction of the forward and backward sweeps.

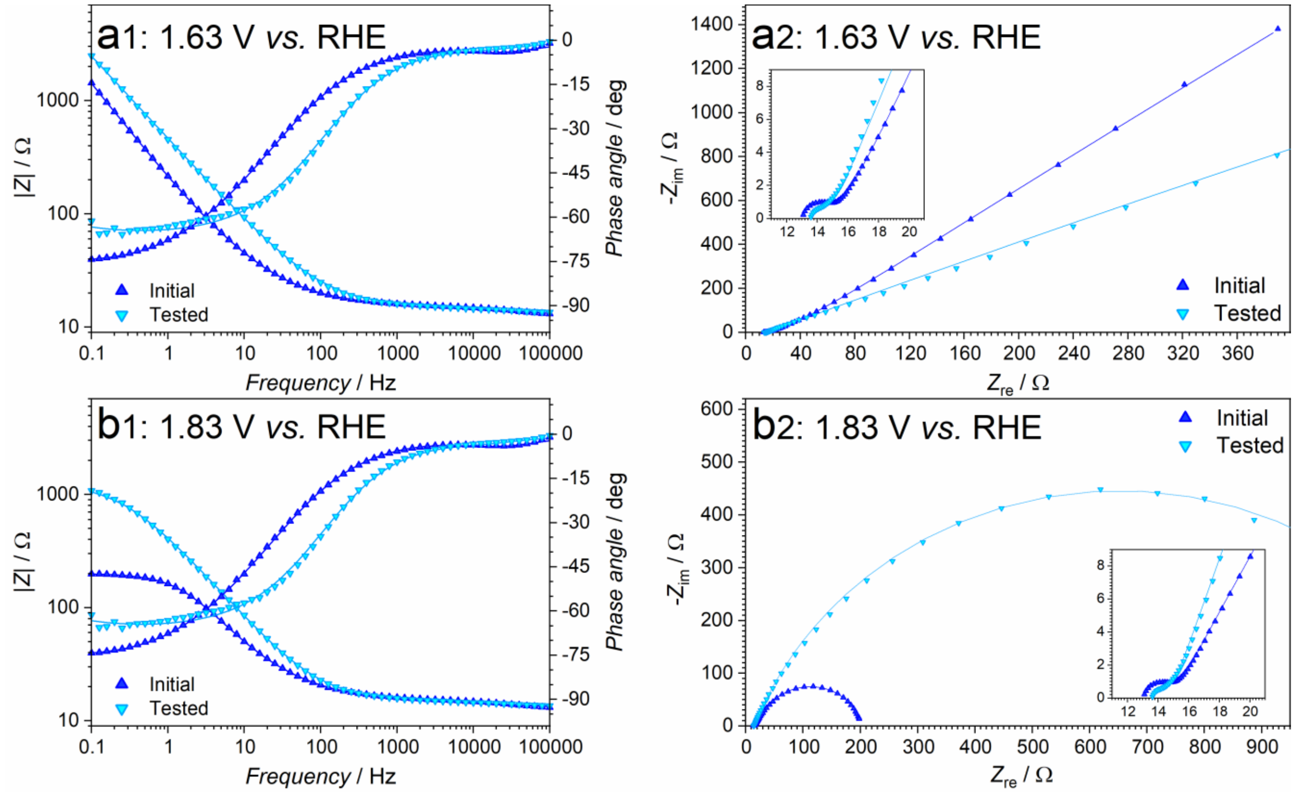

Figure S16. EIS data collected at (a) 1.63 and (b) 1.83 V *vs.* RHE for [Mn+Sb]O_y before (*blue*) and after (*light blue*) OER tests in stirred 0.5 M H_2SO_4 at 24 ± 2 °C (24 h at 10 mA cm^{-2}; 0.5 h at 1.93 V *vs.* RHE; 0.5 h at 2.03 V *vs.* RHE). Symbols show experimental data, while lines show fits based on the models and parameters summarised in Table S2. Insets to the Nyquist plots show higher frequency components representing the FTO|catalyst interface with possible contributions from interfaces between grains and/or different phases within the catalyst layer; main plots show the major charge-transfer resistance||double-layer capacitance component.

Table S2. EIS fitting parameters for the data in Figure S16 collected for [Mn+Sb]O_y.[a]

E / V *vs.* RHE		R_u / Ω	R_1 / Ω	Q_1 / µF s^{a_1-1}	a_1	R_2 / Ω	Q_2 / µF s^{a_2-1}	a_2	R_{ct} / Ω	Q_{dl} / µF $s^{a_{dl}-1}$	a_{dl}
1.63	initial	13	2.0	22	0.85	27	6800	0.55	1.3×10^5	1000	0.85
	tested	14	1.3	83	0.80	Not used			4.8×10^5	560	0.74[b]
1.83	initial	13	2.1	26	0.84	15	2700	0.65	0.2×10^3	700	0.90
	tested	14	1.3	110	0.78	Not used			1.3×10^3	510	0.78

[a] Where possible, fitting was undertaken using $R_u[R_1||CPE_1][R_{ct}||CPE_{dl}]$ model, where R_u is uncompensated resistance, R_{ct} is charge-transfer resistance of a faradaic process, *viz.* the OER, CPE_{dl} is a constant phase element representing double-layer capacitance, while $[R_1||CPE_1]$ likely represents the FTO|catalyst interface. In some cases, satisfactory fit could be only achieved with the $R_u[R_1||CPE_1][R_2||CPE_2][R_{ct}||CPE_{dl}]$ model, where additional $[R_2||CPE_2]$ element might be associated with the interfaces between grains and/or different phases within the catalyst layer. However, its exact nature is obscure, and no physicochemical significance should be attached to $[R_1||CPE_1]$ and $[R_2||CPE_2]$ in this case. Overall, the presented fitting parameters should be used for semi-quantitative comparisons only. [b] Lower a_{dl} value for the tested *vs.* initial sample is the reason for the apparently higher R_{ct} in the former case, notwithstanding visual comparisons of the "semi-arcs" in Figure S16b might suggest the contrary. However, we emphasise again that the modelling values provided must not be used for any quantitative comparisons, especially when R_{ct} is as high as ~10^5 Ω.

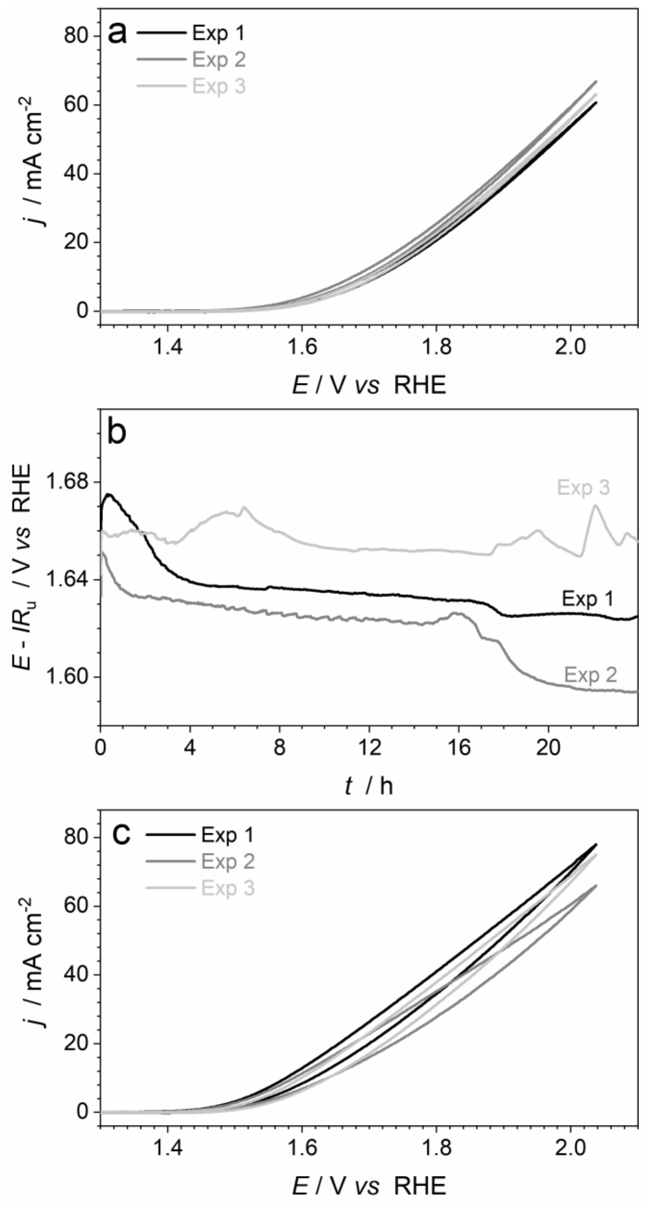

Figure S17. Reproducibility of the electrocatalytic properties of [Ru+Sb]O$_y$ demonstrated for three independent samples tested in 0.5 M H_2SO_4 at 24 ± 2 °C: (a) initial cyclic voltammetry ($\nu = 0.020$ V s^{-1}; potentials are not corrected for ohmic losses), (b) IR_u-corrected chronopotentiograms collected at 10 mA cm$^{-2}_{\mathrm{geom.}}$, and (c) subsequently recorded cyclic voltammetry ($\nu = 0.020$ V s^{-1}; potentials are not IR_u-corrected).

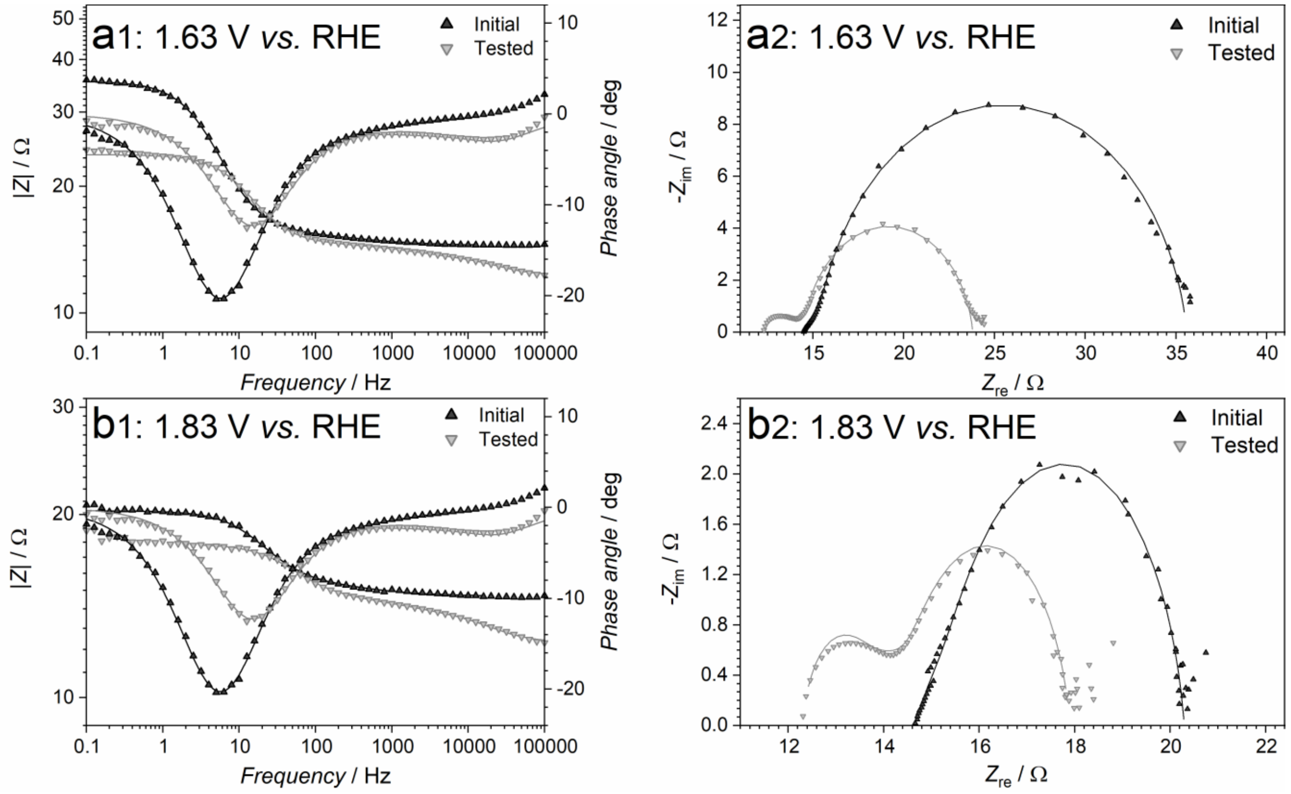

Figure S18. EIS data collected at (a) 1.63 and (b) 1.83 V *vs.* RHE for [Ru+Sb]O_y before (*black*) and after (*grey*) OER tests in stirred 0.5 M H_2SO_4 at 24 ± 2 °C (24 h at 10 mA cm^{-2}; 0.5 h at 1.93 V *vs.* RHE; 0.5 h at 2.03 V *vs.* RHE). Symbols show experimental data, while lines show fits based on the models and parameters summarised in Table S3.

Table S3. EIS fitting parameters for the data in Figure S18 collected for [Ru+Sb]O_y.[a]

E / V *vs.* RHE		R_u / Ω	R_1 / Ω	Q_1 / μF s^{a_1-1}	a_1	R_2 / Ω	Q_2 / μF s^{a_2-1}	a_2	R_{ct} / Ω	Q_{dl} / μF $s^{a_{dl}-1}$	a_{dl}
1.63	initial	15	0.95	5.6×10^3	0.67	Not used			20	3.0×10^3	0.91
	tested	12	1.0	9.6	0.97	1.3	2.1×10^3	0.70	9.2	2.1×10^3	0.92
1.83	initial	15	0.90	8.6×10^3	0.63	Not used			4.7	3.1×10^3	0.89
	tested	12	1.3	18	0.91	1.1	1.2×10^3	0.71	3.3	2.0×10^3	0.88

[a] Where possible, fitting was undertaken using $R_u[R_1||CPE_1][R_{ct}||CPE_{dl}]$ model, where R_u is uncompensated resistance, R_{ct} is charge-transfer resistance of a faradaic process, *viz.* the OER, CPE_{dl} is a constant phase element representing double-layer capacitance, while $[R_1||CPE_1]$ likely represents the FTO|catalyst interface. In some cases, satisfactory fit could be only achieved with the $R_u[R_1||CPE_1][R_2||CPE_2][R_{ct}||CPE_{dl}]$ model, where additional $[R_2||CPE_2]$ element might be associated with the interfaces between grains and/or different phases within the catalyst layer. However, its exact nature is obscure, and no physicochemical significance should be attached to $[R_1||CPE_1]$ and $[R_2||CPE_2]$ in this case. Overall, the presented fitting parameters should be used for semi-quantitative comparisons only.

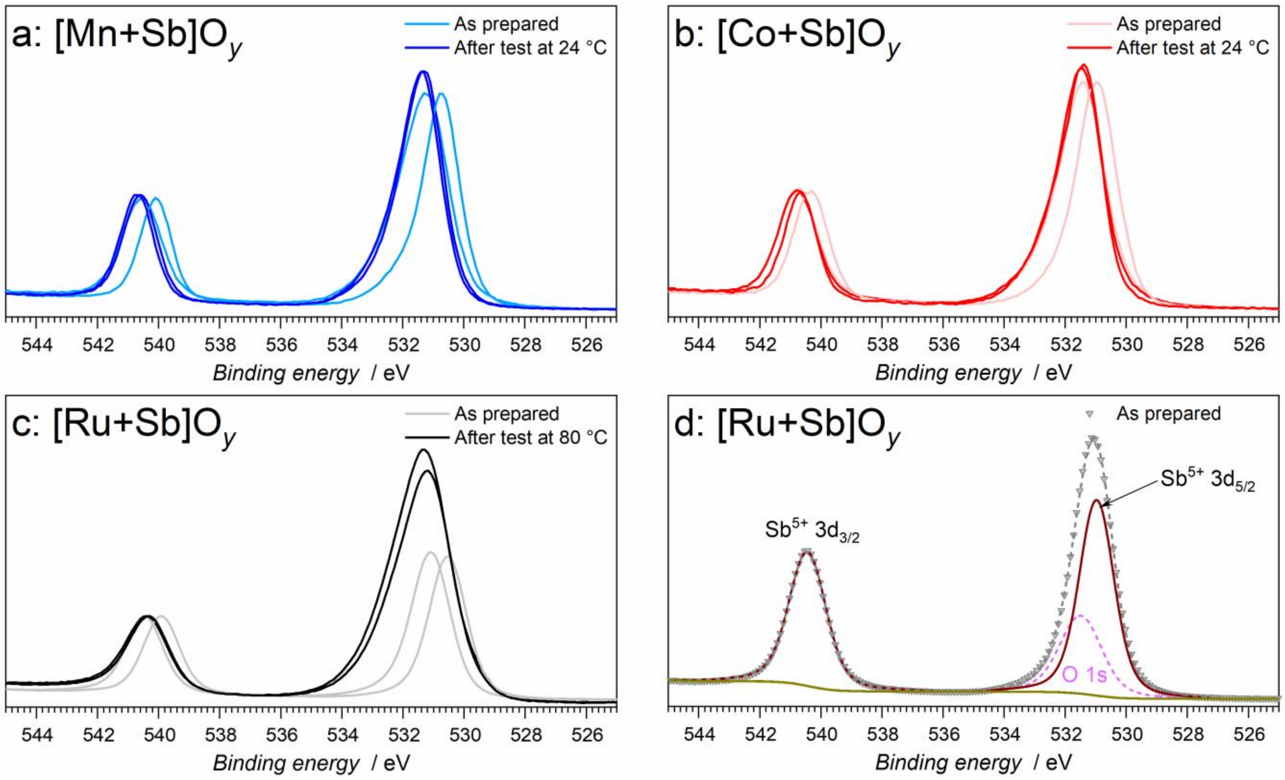

Figure S19. Sb 3d + O 1s spectra for (a) [Mn+Sb]O$_y$, (b) [Co+Sb]O$_y$ and (c) [Ru+Sb]O$_y$ before (*pale traces*) and after (*vivid traces*) electrocatalytic tests in 0.5 M H_2SO_4. Panel (d) shows an example of fitting of the Sb 3d + O 1s spectrum for as-prepared [Ru+Sb]O$_y$ (*triangles*) exhibiting the Sb^{5+} (*brown*) and O 1s (*light magenta*) signals; background is shown as *dark yellow*, while cumulative fitting curve is *dashed grey*. [Mn+Sb]O$_y$ and [Co+Sb]O$_y$ were tested subsequently for 24 h at 10 mA cm^{-2}, 0.5 h at 2.03 V *vs.* RHE, and 0.5 h at 1.93 V *vs.* RHE at ambient temperature; [Ru+Sb]O$_y$ was tested for 10 h at 10 mA cm^{-2} at 80 ± 1 °C. Two curves of each colour in panels (a-c) exemplify the reproducibility of the spectral patterns.

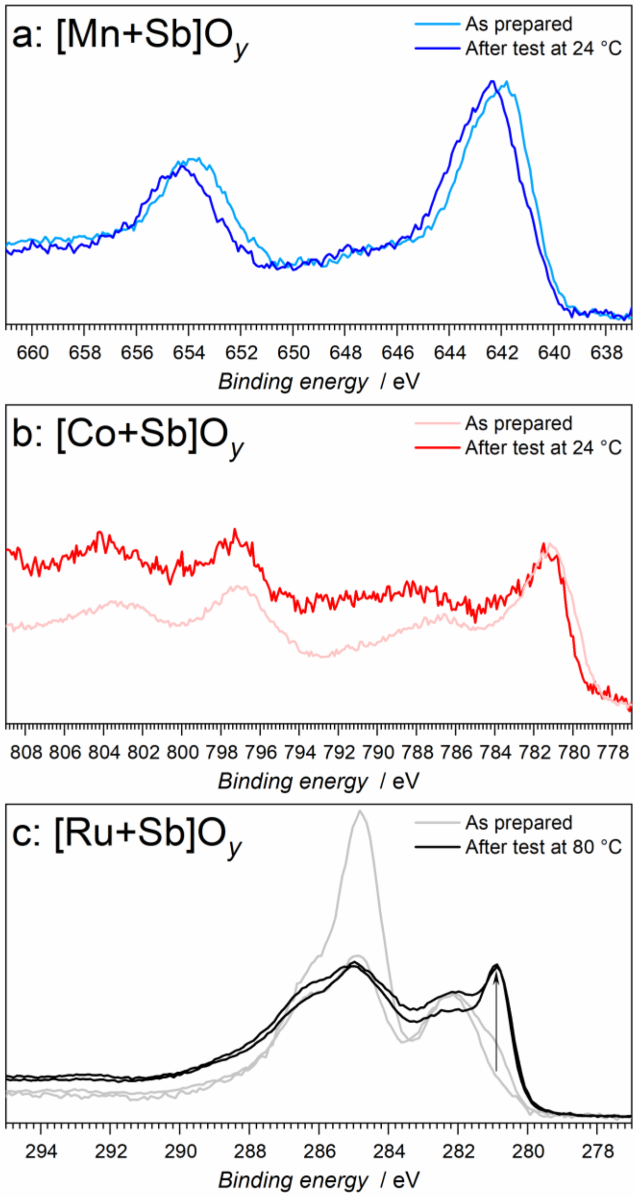

Figure S20. (a) Mn 2p spectra for [Mn+Sb]O$_y$, (b) Co 2p spectra for [Co+Sb]O$_y$ and (c) Ru 3d + C 1s spectra for [Ru+Sb]O$_y$ before (*pale traces*) and after (*vivid traces*) electrocatalytic tests in 0.5 M H_2SO_4. [Mn+Sb]O$_y$ and [Co+Sb]O$_y$ were tested for 24 h at 10 mA cm^{-2} and then for 1 h at 2.03 and 1.93 V *vs.* RHE at ambient temperature; [Ru+Sb]O$_y$ was tested for 12 h at 10 mA cm^{-2} at 80 ± 1 °C. In panel (b), two curves of each colour exemplify the reproducibility of the spectral patterns, while arrow highlights the evolution of the Ru 3d$_{5/2}$ signal ascribed to Ru^{4+}.

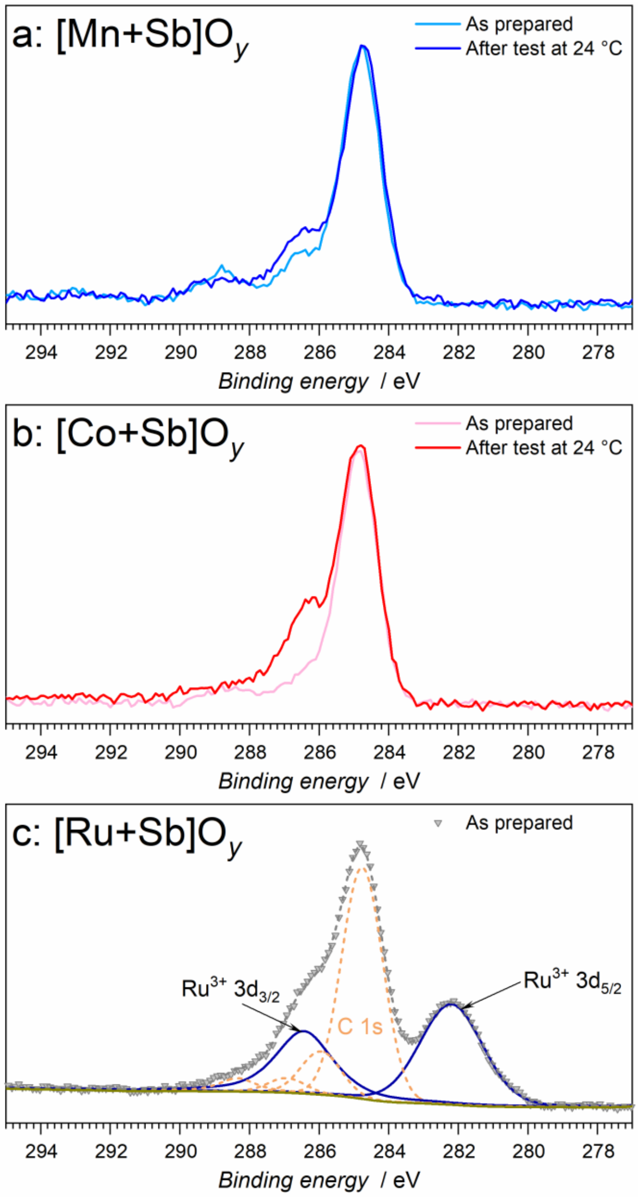

Figure S21. C 1s spectra for (a) [Mn+Sb]O$_y$, and (b) [Co+Sb]O$_y$ before (pale traces) and after (vivid traces) electrocatalytic tests in 0.5 M H_2SO_4 (24 h at 10 mA cm^{-2}, 0.5 h at 2.03 V *vs.* RHE, and 0.5 h at 1.93 V *vs.* RHE at ambient temperature). Panel (c) exemplifies fitting of the Ru 3d + C 1s spectrum for as-prepared Ru+SbO$_y$ (*triangles*) exhibiting the Ru^{3+} (*dark blue*) and C 1s (*yellow*) signals; background is shown as *dark yellow*, while the cumulative fitting curve is *dashed grey*.

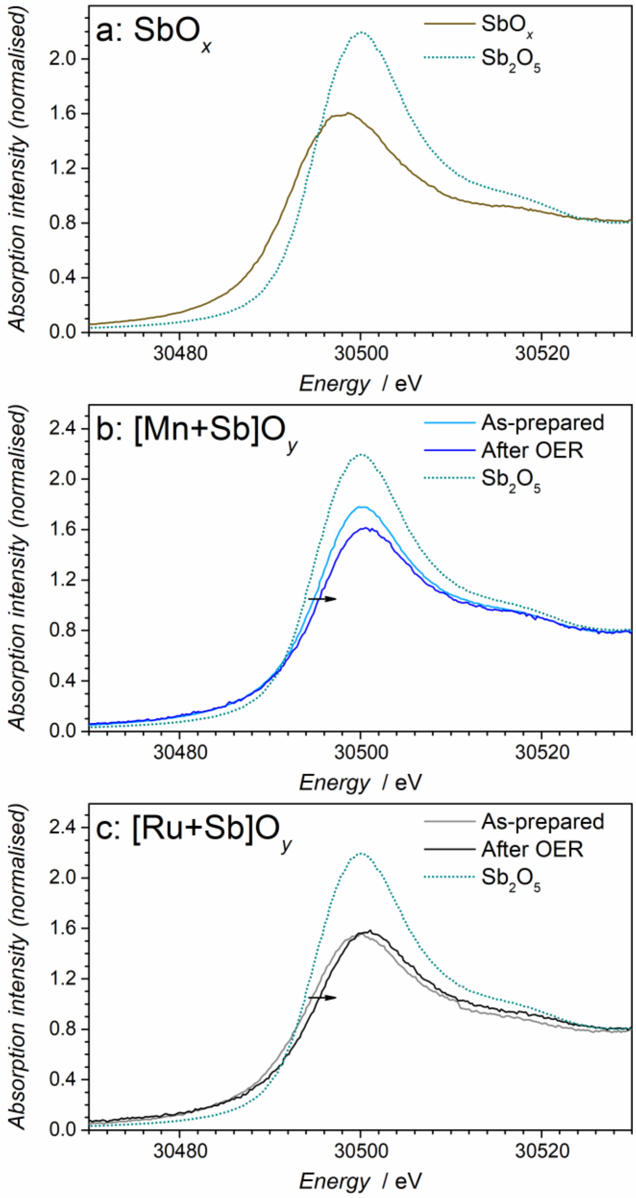

Figure S22. Sb K-edge XANES data for (a) SbO_x (*brown*), (b) $[Mn+Sb]O_y$ before (*light blue*) and after (*blue*) the OER in stirred 0.5 M H_2SO_4 for 24 h at 10 mA cm^{-2} at 24 ± 2 °C and (c) $[Ru+Sb]O_y$ before (*grey*) and after (*black*) the OER in stirred 0.5 M H_2SO_4 for 10 h at 10 mA cm^{-2} at 80 ± 1 °C. Reference data for Sb_2O_5 (*dotted teal*) are also shown. Arrows show slight positive energy shift induced by testing the catalysts.

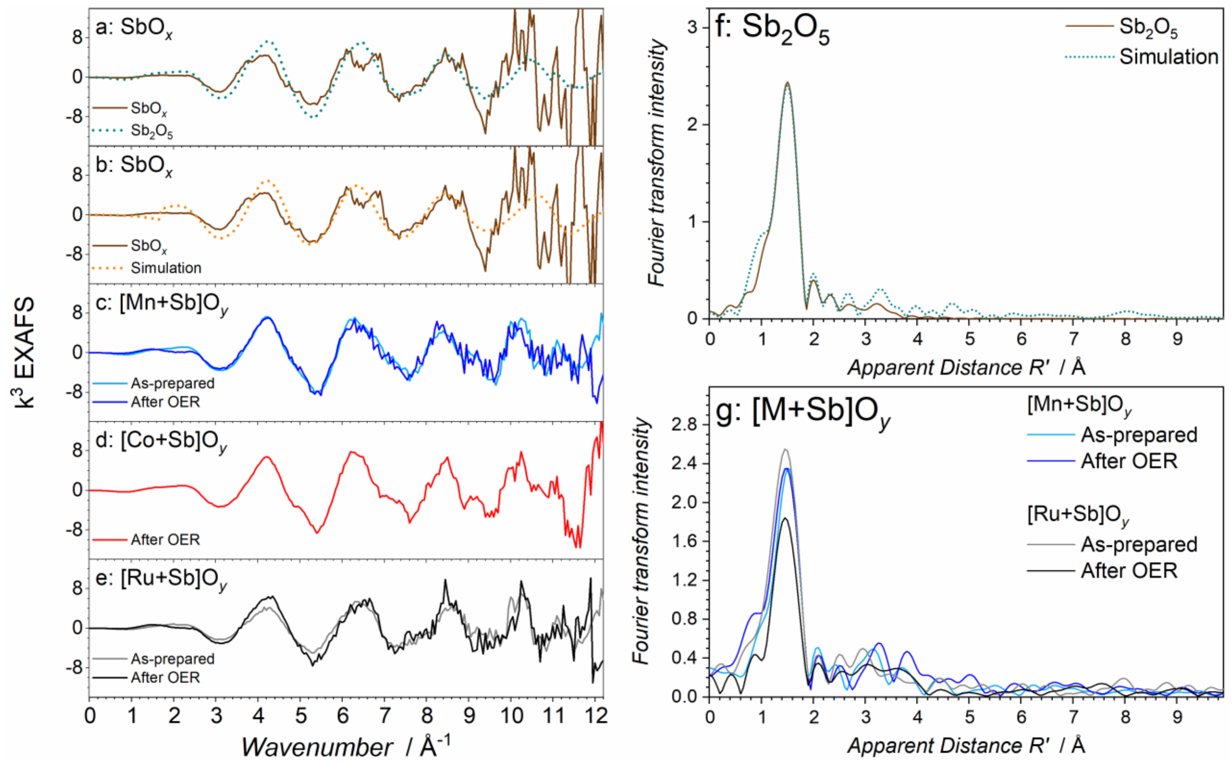

Figure S23. Sb K-edge EXAFS data for (a) SbO$_x$ (*brown*), (b) Sb$_2$O$_5$ (*teal*) (c) [Mn+Sb]O$_y$ before (*light blue*) and after (*blue*) the OER, (d) [Co+Sb]O$_y$ after the OER(*red*), and (e) [Ru+Sb]O$_y$ before (*grey*) and after (*black*) the OER. Fourier transform of the Sb K-edge EXAFS is shown for (f) Sb$_2$O$_5$ as well as for (g) [Mn+Sb]O$_y$ and [Ru+Sb]O$_y$ before (*pale traces*) and after (*vivid traces*) tests. Panel (a) additionally shows reference data for Sb$_2$O$_5$ (*dotted teal*), while panels (b) and (f) feature a simulation (*dotted orange*) based on the parameters in Table S1. [Mn+Sb]O$_y$ and [Co+Sb]O$_y$ were tested in stirred 0.5 M H$_2$SO$_4$ for 24 h at 10 mA cm^{-2} at 24 ± 2 °C; [Ru+Sb]O$_y$ was tested in stirred 0.5 M H$_2$SO$_4$ for 10 h at 10 mA cm^{-2} at 80 ± 1 °C.

Table S4. Crystal structure parameters used for the EXAFS simulations to fit the experimental data for Sb$_2$O$_5$ shown in Figure S23.

Atomic Pair	Number	Distance / Å		Debye-Waller (s2)
		Tabulated [b]	Simulation	
Sb-O	3	1.91	1.95(1)	0.001(1)
Sb-O	3	2.10	2.10(1)	0.001(1)
Sb-Sb	3	3.24	3.24(4)	0.02(1)
Sb-Sb	2	3.42	3.42(6)	0.02(1)

[a] Other parameters: *S02* = 1.30 ± 0.13, *E0* = 5.6 ± 1.3 eV, R-factor = 0.009. [b] As reported in Ref.[S9]

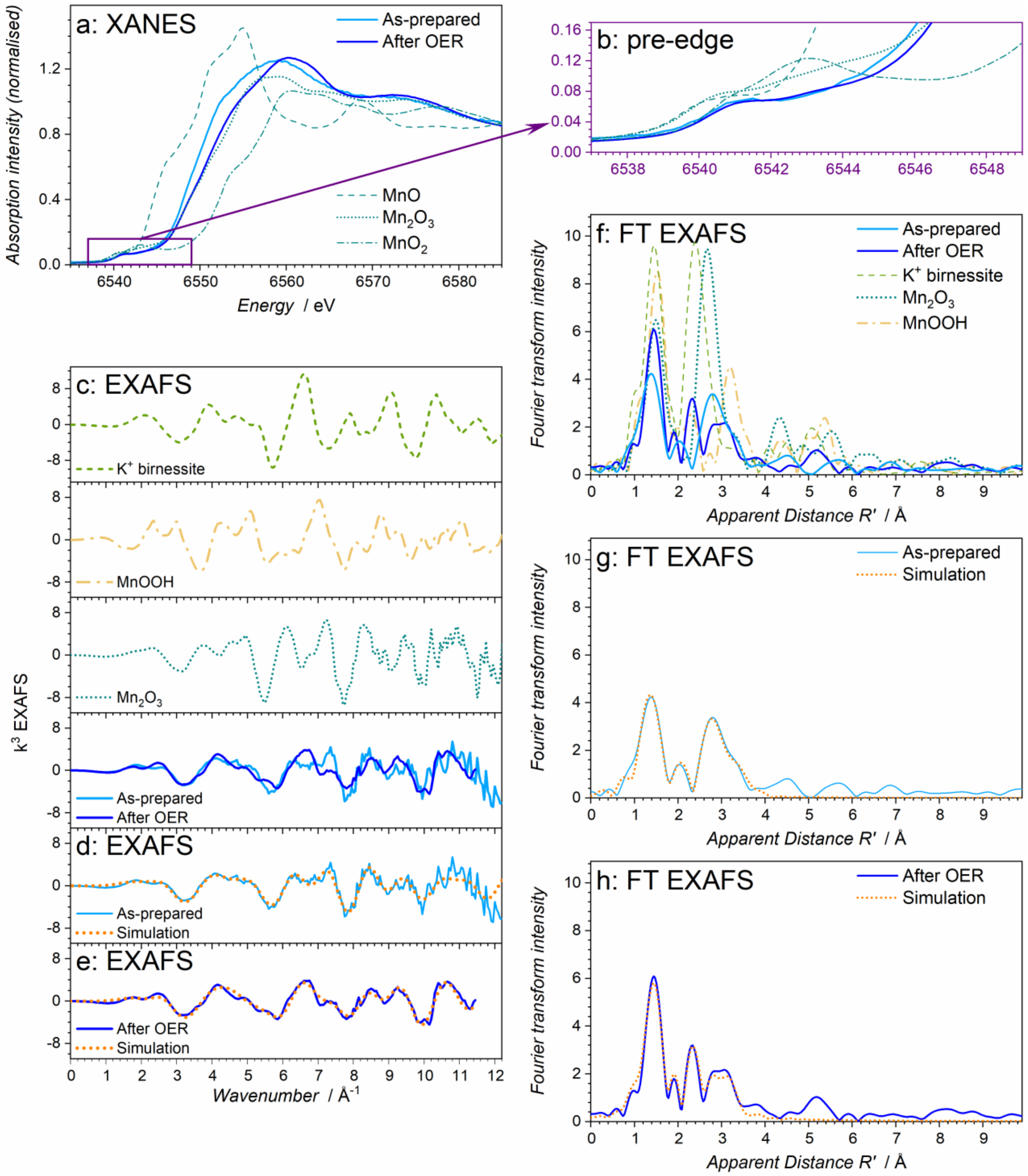

Figure S24. Mn K-edge XAS data for [Mn+Sb]O_y before (*light blue*) and after (*blue*) OER test in stirred 0.5 M H_2SO_4 for 24 h at 10 mA cm^{-2} at 24 ± 2 °C: (a) XANES, (b) XANES pre-edge, (c-e) EXAFS, (f-h) Fourier transform of the EXAFS. Panels (a-c) and (f) show reference data for MnO, Mn_2O_3, MnO_2, MnOOH and K^+-birnessite (*dashed/dotted traces*). Panels (d-e) and (g-h) show simulations (*dotted orange*) based on the parameters summarised in Table S5.

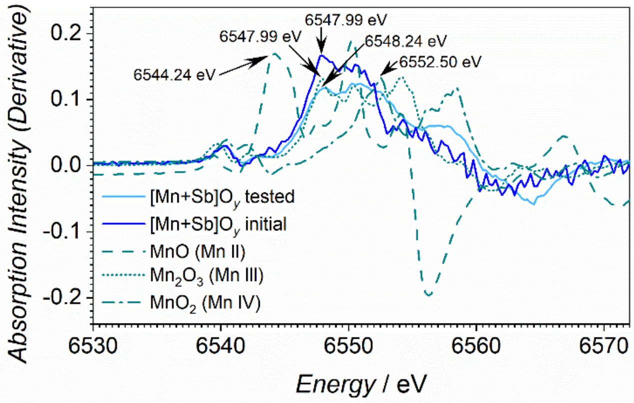

Figure S25. Derivative plots of the Mn K-edge XANES data for [Mn+Sb]O$_y$ before (*light blue*) and after (*blue*) OER test in stirred 0.5 M H_2SO_4 for 24 h at 10 mA cm^{-2} at 24 ± 2 °C along with the reference data for MnO, Mn_2O_3, MnO_2, MnOOH and K^+-birnessite (*dashed/dotted traces*).

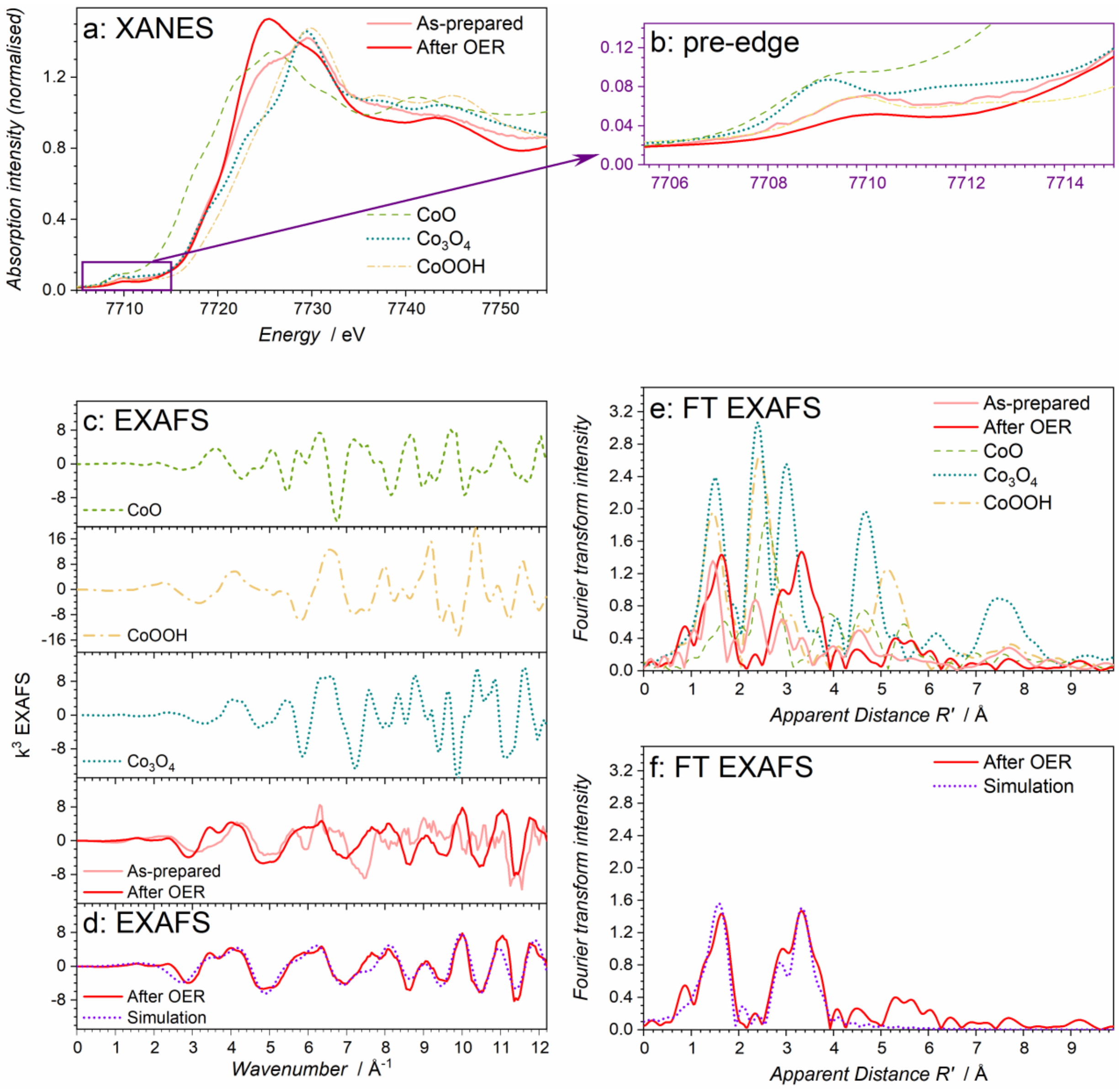

Figure S26. Co K-edge XAS data for [Co+Sb]O_y before (*pink*) and after (*red*) OER test in stirred 0.5 M H_2SO_4 for 24 h at 10 mA cm^{-2} at 24 ± 2 °C: (a) XANES, (b) XANES pre-edge, (c-d) EXAFS, (e-f) Fourier transform of the EXAFS. Panels (a-c) show reference data for CoO, Co_3O_4 and CoOOH (*dashed/dotted traces*). Panels (d) and (f) show simulations (*dotted purple*) based on the parameters summarised in Table S6.

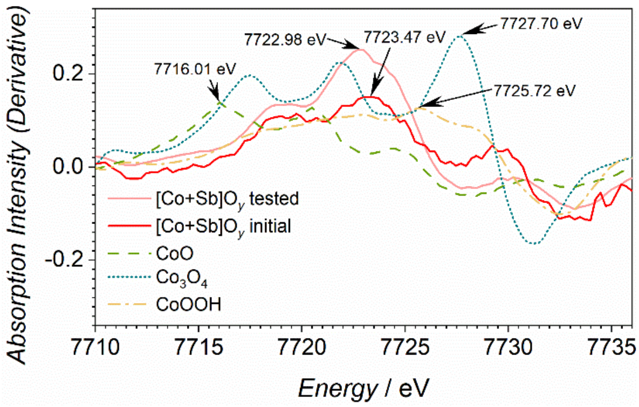

Figure S27. Derivative plots of the Co K-edge XANES data for [Co+Sb]O$_y$ before (*pink*) and after (*red*) OER test in stirred 0.5 M H_2SO_4 for 24 h at 10 mA cm^{-2} at 24 ± 2 °C along with the reference data for CoO, Co_3O_4 and CoOOH (*dashed/dotted traces*).

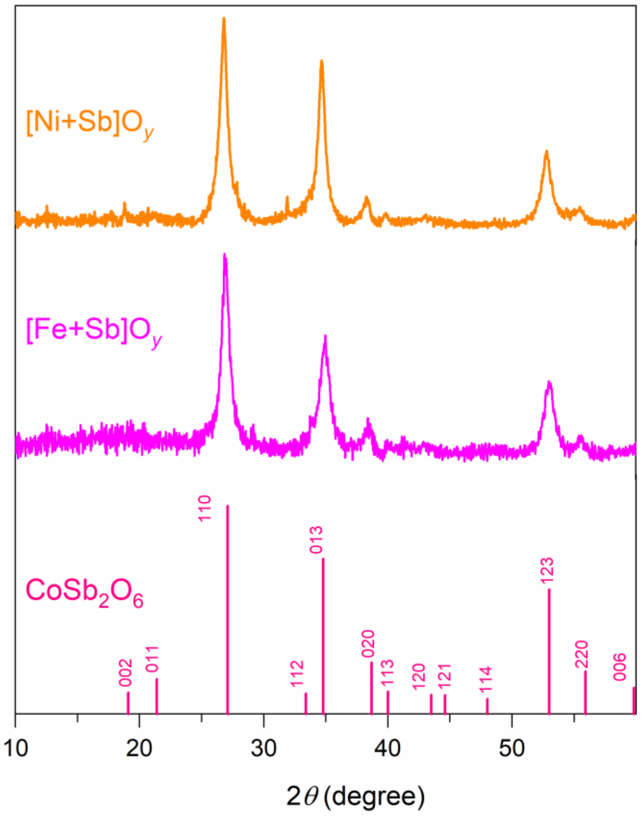

Figure S28. X-ray diffractograms of as-synthesised nickel-antimony (*orange*) and iron-antimony (*magenta*) oxides. Vertical lines show tabulated positions and relative intensities for $CoSb_2O_6$ (ICSD-108964).

Table S5. $MnSb_2O_6$ crystal structure parameters used for the EXAFS simulations to fit the experimental data for $[Mn+Sb]O_y$ shown in Figure S24.

Atomic Pair	Number	Distance / Å		Debye-Waller (σ^2)
		Tabulated [a]	Simulation	
As-prepared [b]				
Mn-O	4	2.124	1.91(2)	0.006(2)
Mn-O	2	2.28	2.18(2)	0.010(15)
Mn-Sb	**2**	**not present [d]**	**2.82(5)**	**0.004(3)**
Mn-Sb	3	3.24	3.23(4)	0.005(7)
Mn-Sb	**3**	**not present [d]**	**3.49(4)**	**0.002(2)**
Mn-Sb	2	3.63	3.61(5)	0.026(11)
After the OER test [c]				
Mn-O	6	2.12	1.88(2)	0.005(2)
Mn-Sb	**2**	**not present [d]**	**2.61(3)**	**0.007(4)**
Mn-Sb	3	3.24	3.21(5)	0.006(9)
Mn-Sb	**2**	**not present [d]**	**3.46(6)**	**0.006(5)**
Mn-Sb	3	3.67	3.61(6)	0.001(8)

[b] As reported in Ref.[S10] [b] Other parameters: *S02* = 0.61 ± 0.14, *E0* = -2.5 ± 1.8 eV, R-factor = 0.0059. [c] Other parameters: *S02* = 0.400, *E0* = -6.8 ± 1.7 eV, R-factor = 0.067. [d] Additional interactions were needed to explain the experimentally observed intensity patterns.

Table S6. $CoSb_2O_6$ crystal structure parameters[a] used for the EXAFS simulations to fit the experimental data for tested $[Co+Sb]O_y$ shown in Figure S26.

Atomic Pair	Number	Distance / Å		Debye-Waller (σ^2)
		Tabulated [b]	Simulation	
Co-O	6	2.00	2.00 [c]	0.006(2)
Co-Sb	2	3.09	3.09 [c]	0.007(3)
Co-Sb	8	3.63	3.63 [c]	0.006(1)
Co..O..Sb	16	3.83	3.83 [c]	0.003(3)

[a] Other parameters: *S02* = 0.79 ± 0.12, *E0* = -6.1 ± 0.9 eV, R-factor = 0.040. [b] As reported in Ref.[S10] [c] These values were set to those in the crystal structure.

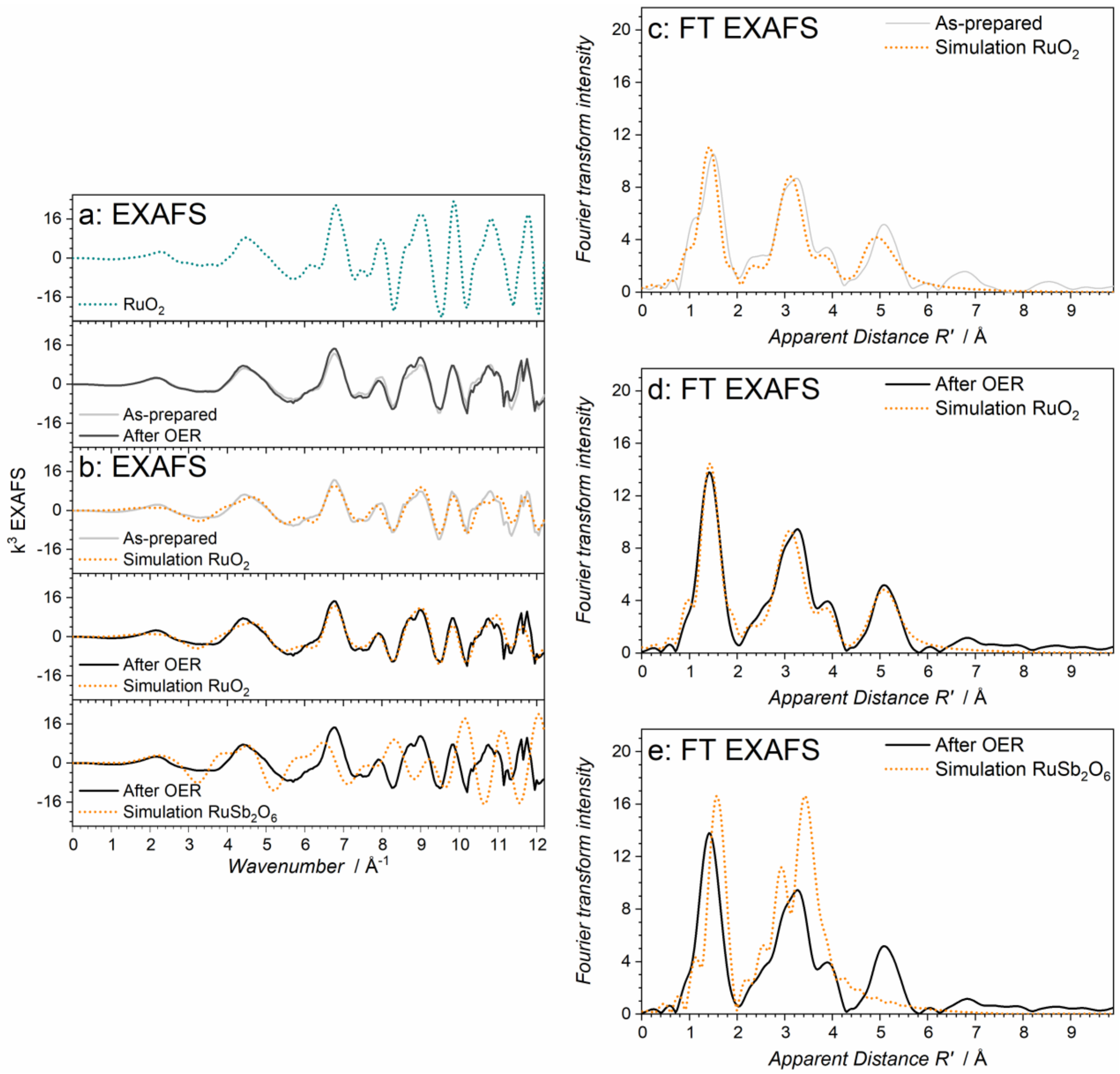

Figure S29. Ru K-edge XAS data for [Ru+Sb]O$_y$ before (*grey*) and after (*black*) OER test in stirred 0.5 M H_2SO_4 for 10 h at 10 mA cm^{-2} at 80 ± 1 °C: (a-b) EXAFS, (c-e) Fourier transform of the EXAFS. Panel (a) shows reference data for RuO_2 (*dotted teal*). Panels (b-f) show simulations (*dotted orange*) based on RuO_2 and $RuSb_2O_6$ and on the parameters summarised in Table S4.

Table S7. RuO_2 and $RuSb_2O_6$ crystal structure parameters used for the EXAFS simulations to fit the experimental data for [Ru+Sb]O_y shown in Figure S29.

Atomic Pair	Number	Distance / Å		Debye-Waller (σ^2)
		Tabulated [a]	Simulation	
As-prepared [b]				
		RuO_2		
Ru-O	6	1.94	1.94(2)	0.004(1)
Ru-Ru	2	3.11	3.11(3)	0.004(3)
Ru-Ru	8	3.53	3.53(3)	0.005(1)
Ru-Ru	4	4.49	4.45(5)	0.005(4)
Ru-Ru	8	5.46	5.41(3)	0.002(1)
Ru..O..Ru	16	5.64	5.64(2)	0.013(13)
After the OER test				
		RuO_2 [c]		
Ru-O	6	1.94	1.94 (2)	0.002(1)
Ru-Ru	2	3.11	3.11(3)	0.003(3)
Ru-Ru	8	3.53	3.53(3)	0.004(2)
Ru-Ru	4	4.49	4.46(5)	0.004(5)
Ru-Ru	8	5.46	5.46(2)	0.005(9)
Ru..O..Ru	16	5.64	5.62(2)	0.005(9)
		$RuSb_2O_6$ [d]		
Ru-O	6	2.00	2.00	0.002
Ru-Sb	2	3.09	3.09	0.002
Ru-Sb	8	3.63	3.63	0.006
Ru-Sb..O	16	3.83	3.83	0.006

[a] As reported in Ref.[S11] for RuO_2; $RuSb_2O_6$ model was developed based on Ref.[S10] [b] Other parameters: *S02* = 0.91 ± 0.05, *E0* = -10.1 ± 1.0 eV, R-factor = 0.070. [c] Other parameters: *S02* = 0.912 (not floated in the final fit), *E0* = -10.1 ± 1.0, R-factor = 0.14; [d] Other parameters: *S02* = 0.912 (not floated in the final fit), *E0* = 5.7 ± 1.5 eV, R-factor = 200; parameters in this fit were not optimised due to the lack of any agreement between experiment and simulation, as discussed in the main text.

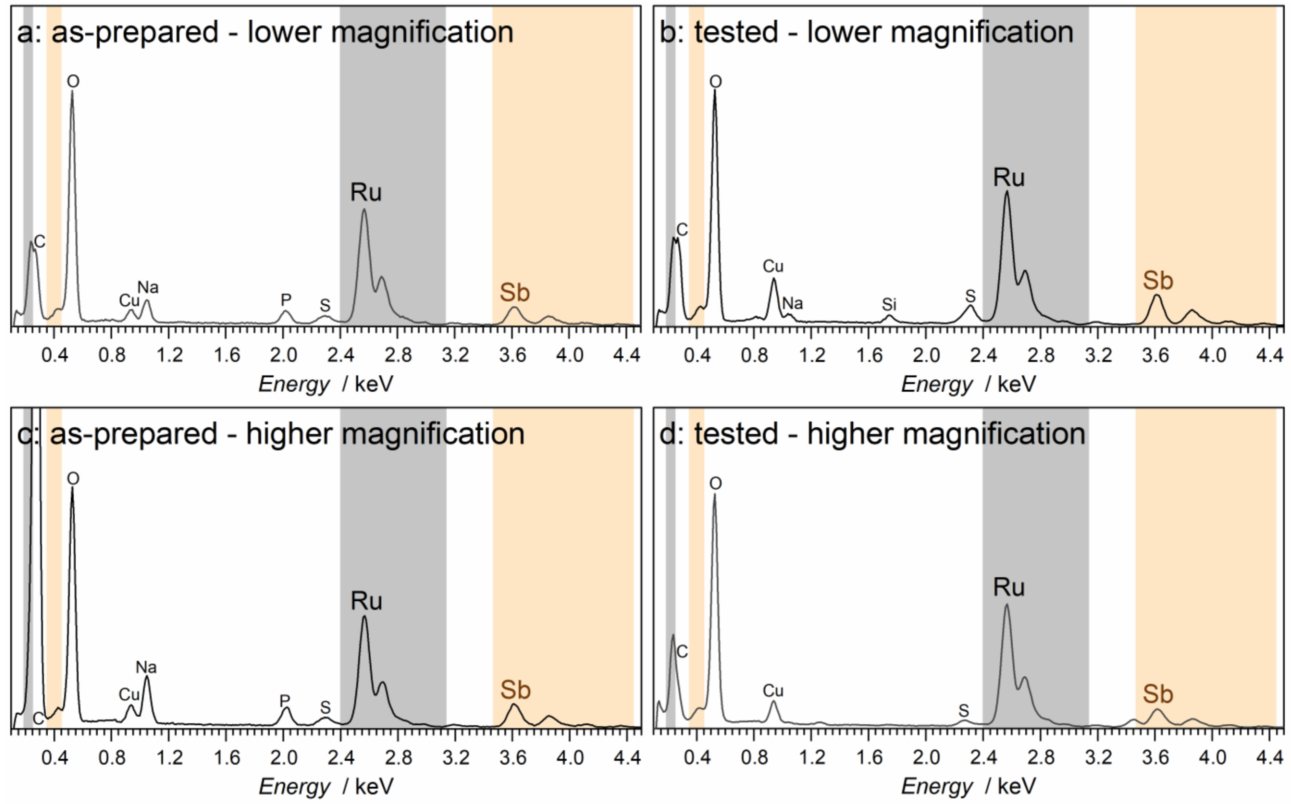

Figure S30. Examples of the energy dispersive X-ray spectra collected during the (a-b) lower and (c-d) higher magnification STEM-EDS mapping for [Ru+Sb]O_y. (a, c) before and (b, d) after test at 10 mA cm^{-2} for 24 h at 80 ± 1 °C. Cu signal is attributed to the TEM grid. Si, Na, P and S signals are associated with the unknown admixtures, which have been most probably introduced during detaching the catalyst material off the FTO-coated glass slides for the TEM sample preparation.

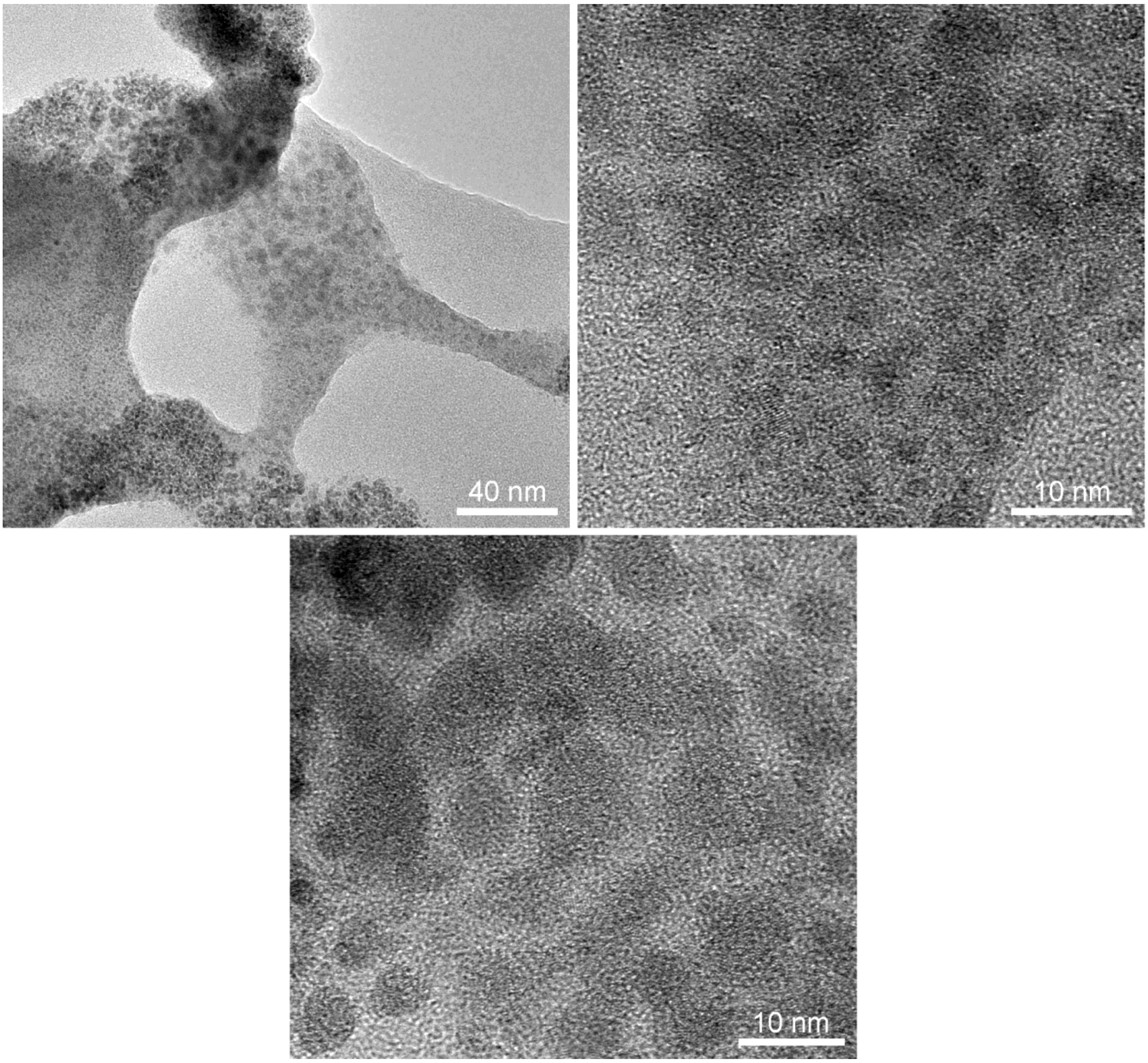

Figure S31. TEM imaging of as-prepared [Ru+Sb]O_y at different magnification.

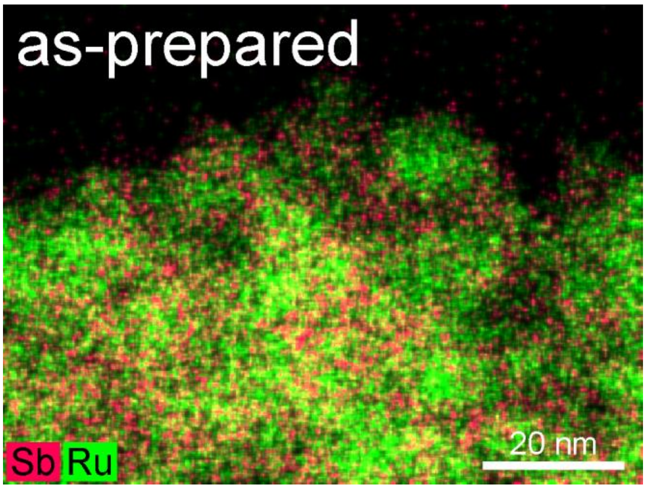

Figure S32. High-magnification STEM-EDS mapping of the as-prepared [Ru+Sb]O$_y$ catalyst.

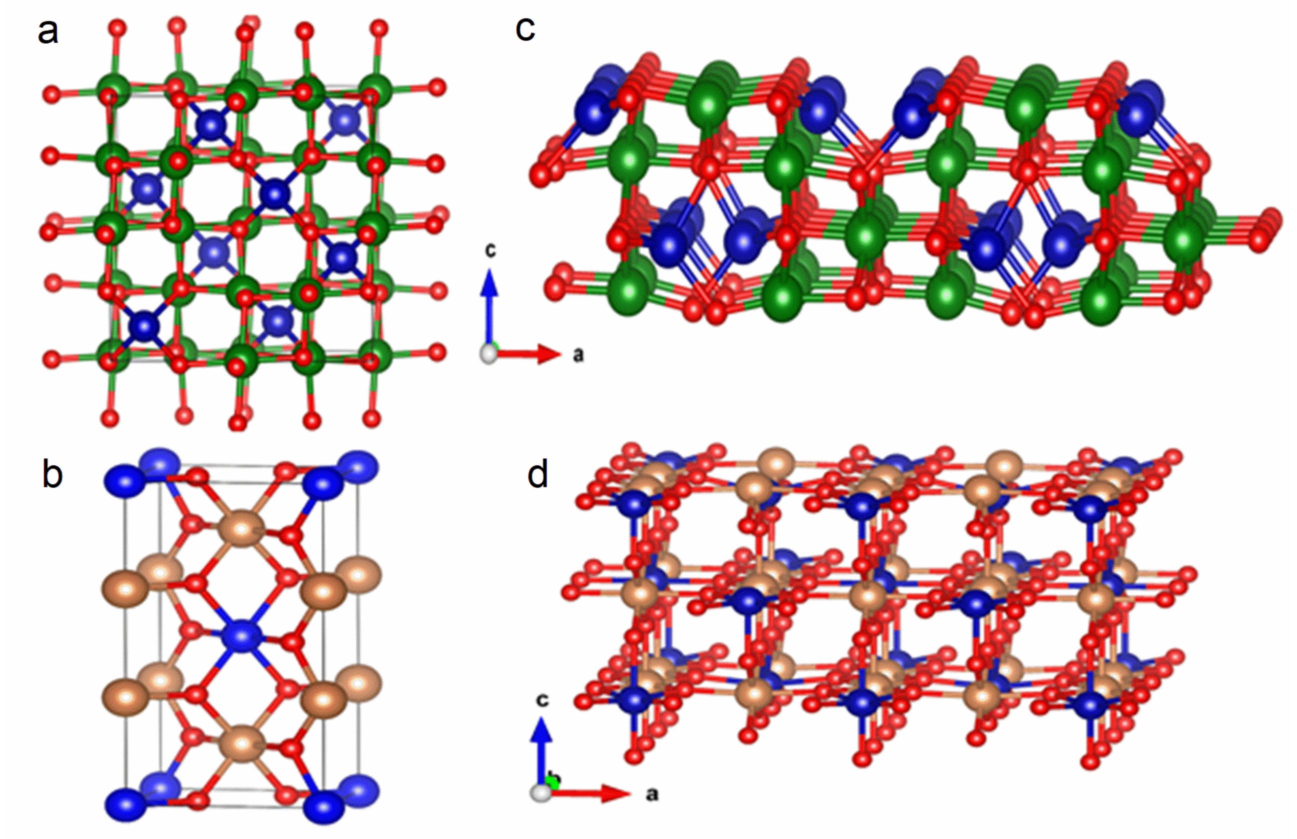

Figure S33. Model crystal structures of (a) Co_3O_4 [$Co^{2+}(Co^{3+})_2O_4$] and (b) $CoSb_2O_6$ [$Co^{2+}(Sb^{5+})_2O_6$], and surface models for (c) (110)-A Co_3O_4 and (d) (110) $CoSb_2O_6$ (*blue*, *green*, *orange* and *red* spheres show Co^{2+}, Co^{3+}, Sb^{5+} and O^{2-}, respectively).

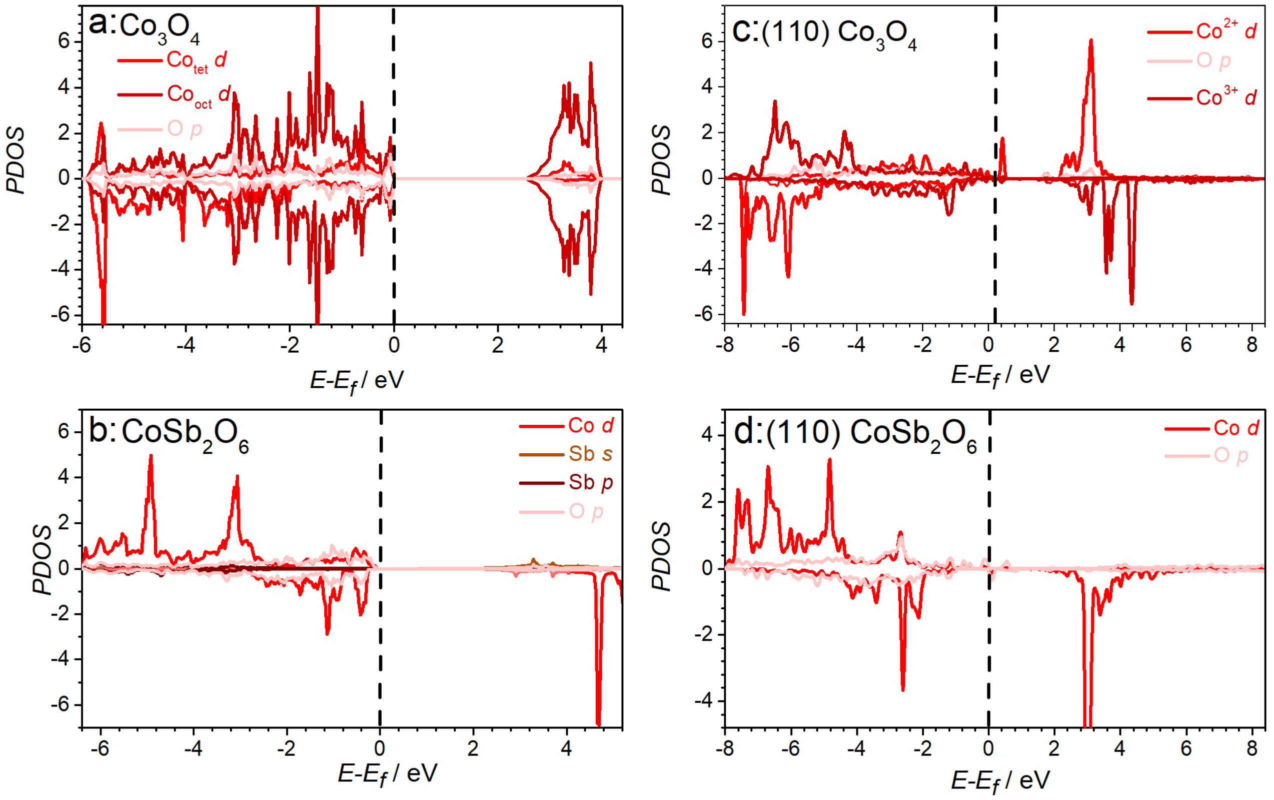

Figure S34. Spin polarised atom/orbital projected partial density of states (PDOS) for bulk (a) Co_3O_4 and (b) $CoSb_2O_6$ and surface (c) (110)-A Co_3O_4 and (d) (110) $CoSb_2O_6$. Fermi levels are set at 0 eV (indicated by vertical dashed lines).

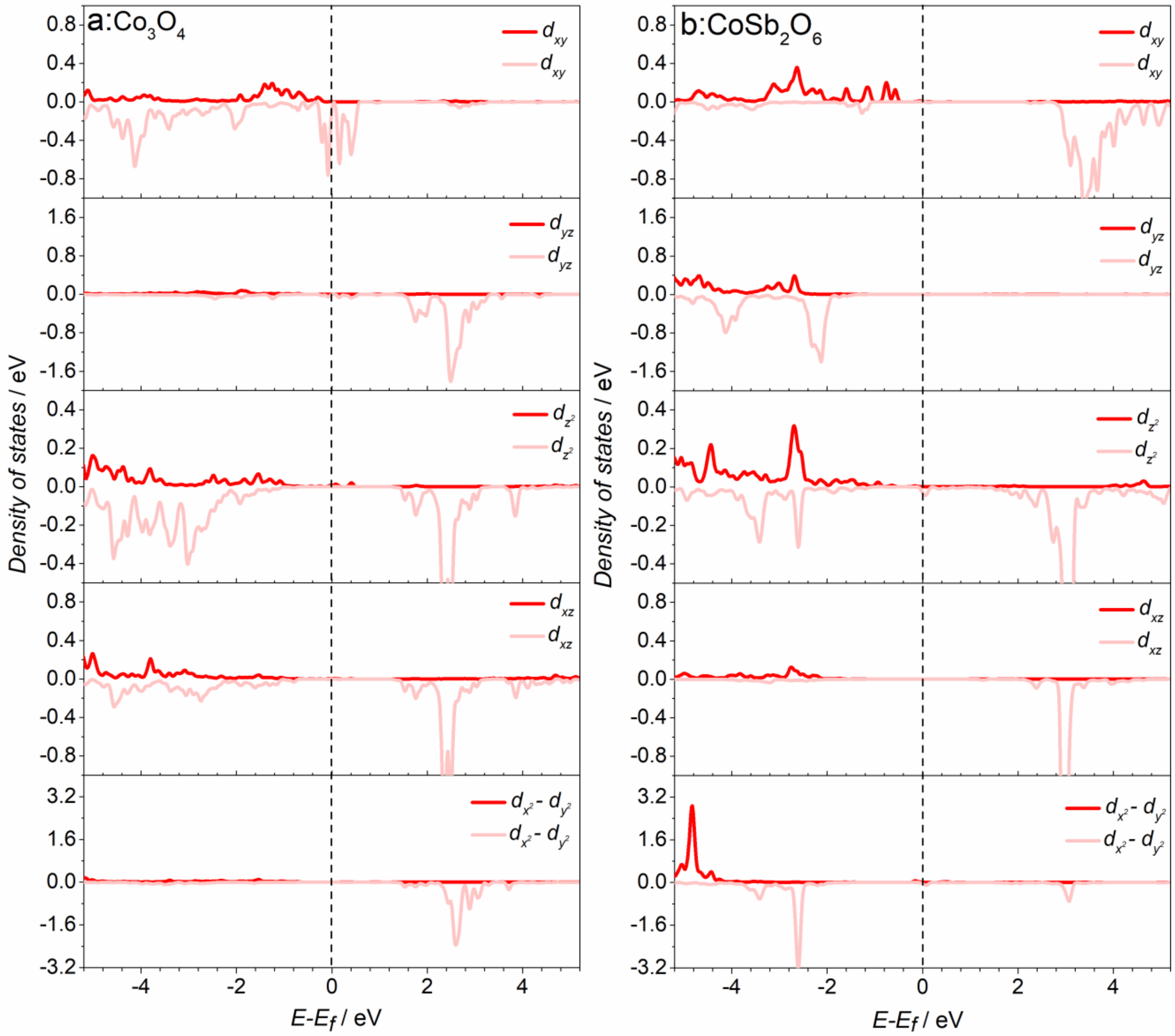

Figure S35. PDOS of Co 3d sub-orbitals d_{xy}, d_{xz}, d_{yz}, d_{z2} and d_{x2-y2} for (a) (110)-A Co_3O_4 and (b) (110) $CoSb_2O_6$ surface models. Fermi levels are set at 0 eV (indicated by vertical lines). The DOS of spin down channel of d_{xy}, d_{yz} and d_{xz} of Co d states has finite value at the Fermi level of Co_3O_4; in $CoSb_2O_6$, the Co d state intensity near and at the Fermi level is substantially diminished. This suggests facilitated charge transfer from Co of $CoSb_2O_6$ to its neighbouring oxygen atoms, which is indicative of the improved bond strength.

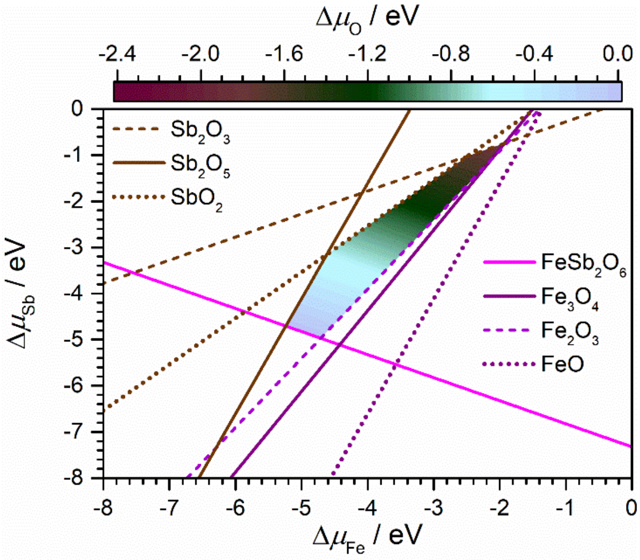

Figure S36. Simulated compositional phase diagram of $FeSb_2O_6$ against individual oxides. Shaded area corresponds to the stable region of $FeSb_2O_6$, where the colour scale shows the allowed chemical potentials for oxygen; coloured lines and the corresponding spaces opposite to the shaded region present the stable regions of the identified individual oxides.

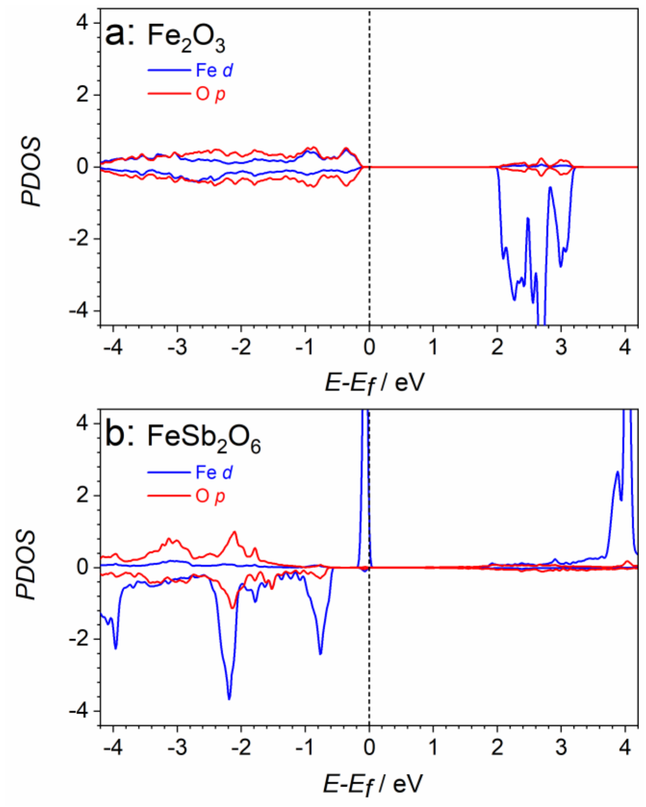

Figure S37. Spin polarised atom/orbital projected partial density of electronic states (PDOS) for bulk (a) Fe_2O_3 and (b) $FeSb_2O_6$. Fermi levels are set at 0 eV.

Table S8. Enthalpies of formation of the [Ru_n+Sb_m]O_y phases considered for the oxygen grand potential diagram.

Composition	ΔH_f (eV per f.u.)	Composition	ΔH_f (eV per f.u.)
Ru	0	**Ru:SbO_2** [b]	
Sb	0	Ru_2:$Sb_{30}O_{64}$	-136.5754
O	0	Ru_4:$Sb_{28}O_{64}$	-132.4576
Individual oxides		Ru_6:$Sb_{26}O_{64}$	-129.6658
SbO_2	-4.3953	Ru_8:$Sb_{24}O_{64}$	-126.56
Sb_2O_3	-7.1036	Ru_{10}:$Sb_{22}O_{64}$	-123.4152
Sb_2O_5	-9.4111	Ru_{12}:$Sb_{20}O_{64}$	-120.1204
RuO_2	-3.4289	Ru_{14}:$Sb_{18}O_{64}$	-117.4506
RuO_4	-4.2085	Ru_{16}:$Sb_{16}O_{64}$	-114.6668
Stoichiometric phases		**Ru:Sb_2O_3** [b]	
$RuSb_2O_6$	-11.6643	Ru_1:$Sb_{31}O_{48}$	-110.3403
$RuSb_2O_5$	-9.6335	Ru_2:$Sb_{30}O_{48}$	-107.1917
$RuSb_4O_{12}$	-20.7176	Ru_4:$Sb_{28}O_{48}$	-101.44
$Ru_2Sb_2O_9$	-12.346	Ru_6:$Sb_{26}O_{48}$	-94.4664
$Ru_{10}Sb_{10}O_{34}$	-57.539	Ru_8:$Sb_{24}O_{48}$	-91.672
$Ru_8Sb_8O_{28}$	-48.5294	Ru_{10}:$Sb_{22}O_{48}$	-85.4024
$Ru_2Sb_2O_8$	-14.4598	Ru_{12}:$Sb_{20}O_{48}$	-82.3354
$Ru_2Sb_2O_7$	-13.2396	Ru_{14}:$Sb_{18}O_{48}$	-76.8166
$RuSb_2O_7$	-11.0804	Ru_{16}:$Sb_{16}O_{48}$	-74.3198
Sb:RuO_2[a]		**Ru:Sb_2O_5** [b]	
Sb_1:$Ru_{15}O_{32}$	-55.6121	Ru_1:$Sb_{15}O_{40}$	-73.5697
Sb_2:$Ru_{14}O_{32}$	-55.939	Ru_2:$Sb_{14}O_{40}$	-70.9568
Sb_2:$Ru_{12}O_{32}$	-57.6568	Ru_4:$Sb_{12}O_{40}$	-70.249
Sb_6:$Ru_{10}O_{32}$	-59.0276	Ru_6:$Sb_{10}O_{40}$	-67.0202
Sb_8:Ru_8O_{32}	-60.5614	Ru_8:Sb_8O_{40}	-63.7794

[a] Sb-doped RuO_2; [b] Ru-doped antimony oxides.

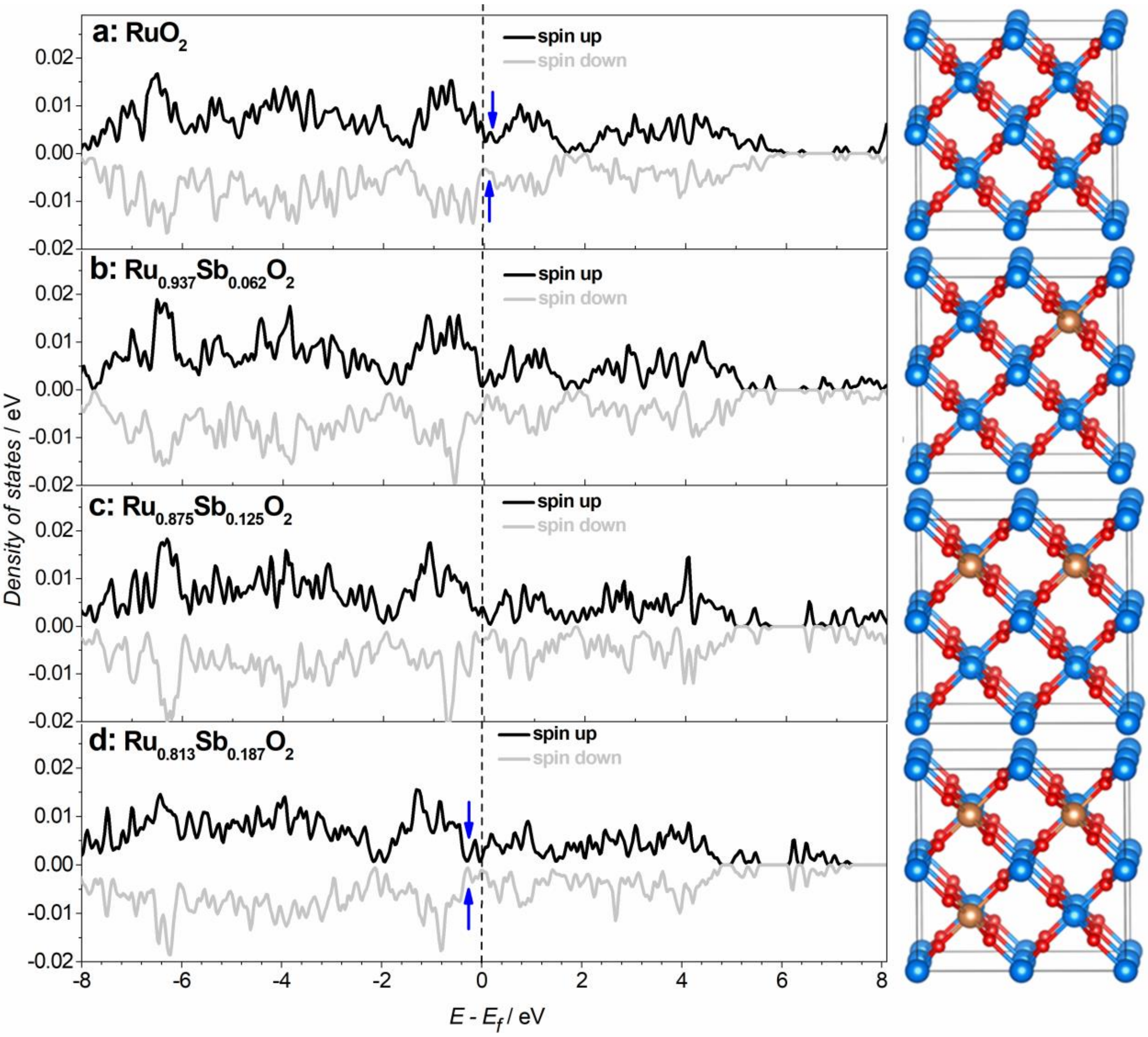

Figure S38. Spin polarised total density of states (TDOS) for (a) RuO_2, (b) $Sb_{0.0625}$:$Ru_{0.9375}O_2$, (c) $Sb_{0.125}$:$Ru_{0.875}O_2$, and (d) $Sb_{0.187}$:$Ru_{0.813}O_2$. Fermi levels are set at 0 eV (indicated by vertical dashed lines). Blue arrows indicate unoccupied states which are filled up and shifted to lower energy. This might be attributed to replacement of Ru^{4+} by higher valency Sb^{5+} atoms as discussed in the main text. Corresponding supercells are shown against the plots on the right (*light blue*, *orange* and *red* spheres show Ru^{2+}, Sb^{5+} and O^{2-}, respectively).

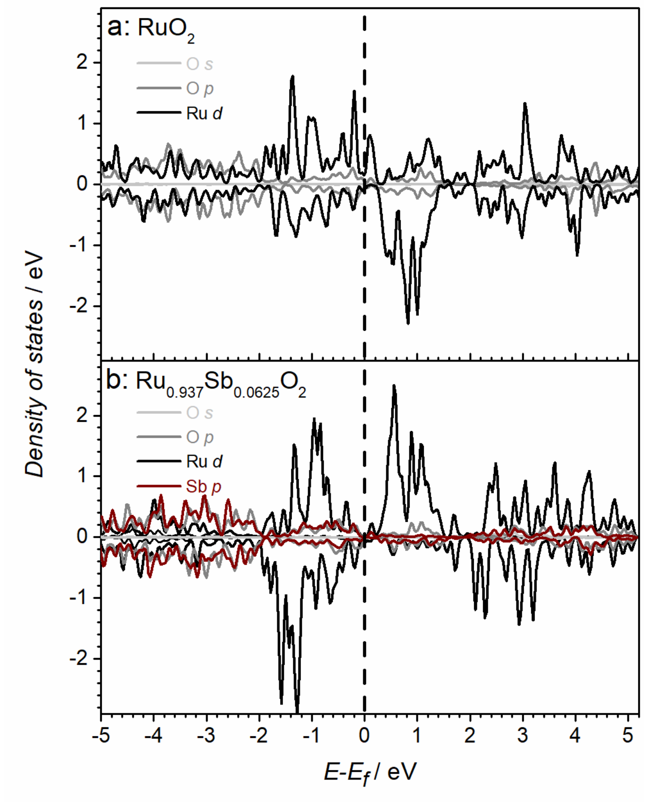

Figure S39. PDOS of (a) RuO_2 and (b) $Sb_{0.0625}$:$Ru_{0.9375}O_2$. Fermi levels are set at 0 eV (indicated by vertical dashed lines). Enhanced overlap of Ru d and O p orbitals near the Fermi level induced by doping with antimony suggests enhanced Ru-O interaction.

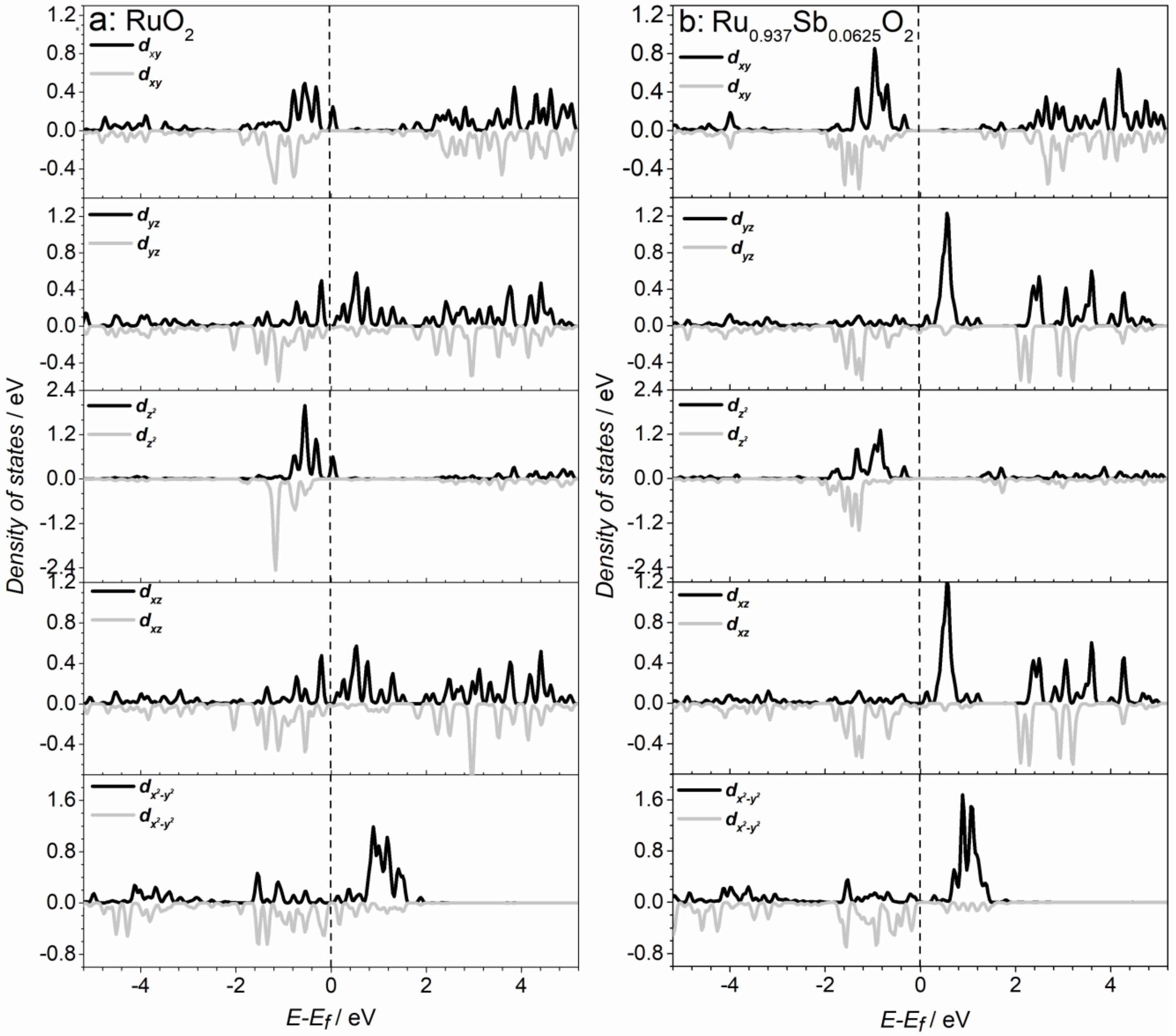

Figure S40. Spin polarised PDOS of Ru 4d sub-orbitals d_{xy}, d_{xz}, d_{yz}, d_{z2} and d_{x2-y2} for (a) RuO_2 and (b) $Sb_{0.0625}$:$Ru_{0.9375}O_2$. Fermi levels are set at 0 eV (indicated by vertical dashed lines). Upon doping of RuO_2 with antimony, states near the Fermi level of d_{yz}, d_{xz} and d_{z2} diminish, which indicates the enhanced electron donation from Ru to O and thus implies stronger Ru-O interaction.

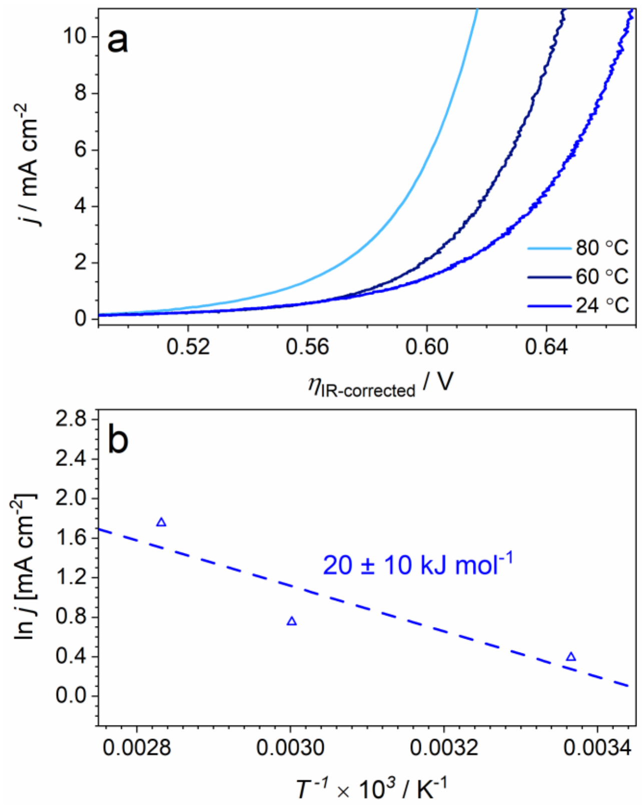

Figure S41. (a) IR_u-corrected backward sweeps of quasi-stabilised cyclic voltammograms for the [Mn+Sb]O_y-catalyzed OER in 0.5 M H_2SO_4 at 24 ± 2 (*blue*), 60 (*dark blue*) and 80 ± 1 °C (*light blue*). (b) Arrhenius plots constructed based on the data in panel (a) for the OER overpotential of 0.6 V (see figure). Dashed lines show tentative linear approximations, while values show corresponding estimates of the apparent activation energy.

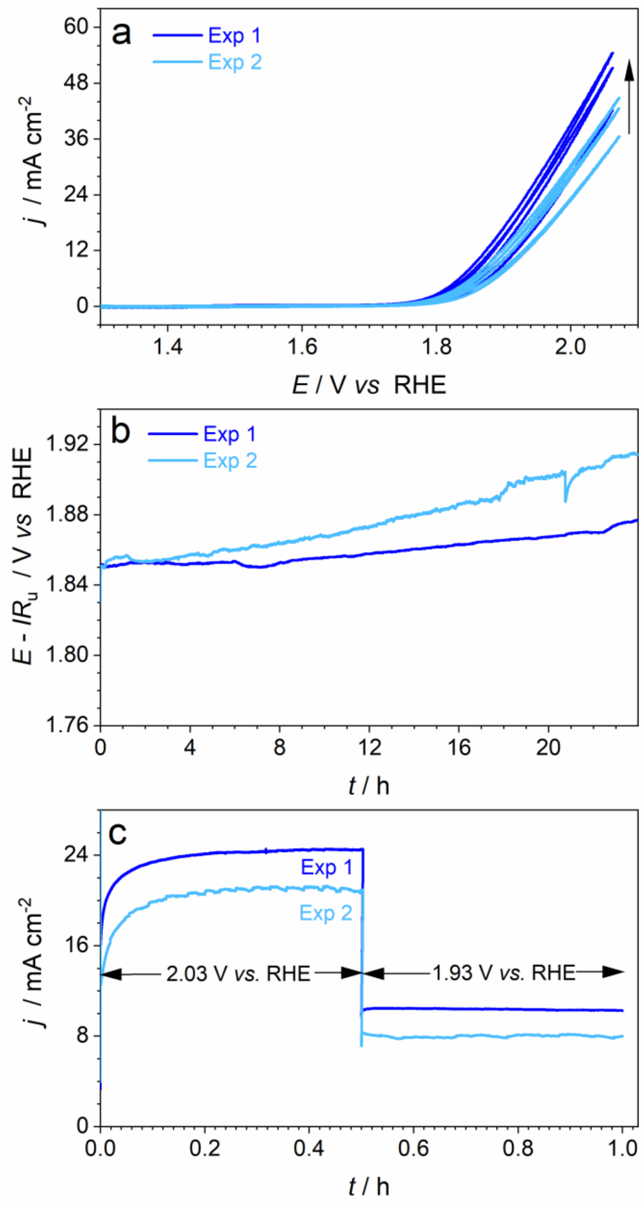

Figure S42. Reproducibility of the OER catalytic activity of $[Mn+Sb]O_y$ in 0.5 M H_2SO_4 at 60 °C: (a) cyclic voltammetry (scan rate 0.020 V s^{-1}; potentials are not corrected for ohmic losses), (b) IR_u-corrected chronopotentiograms at 10 mA $cm^{-2}_{geom.}$, and (c) subsequently recorded chronoamperograms at 2.03 and 1.93 V *vs.* RHE. Current are normalised to the geometric surface area of the electrodes. Arrows in panel (a) show the evolution of voltammograms with cycling.

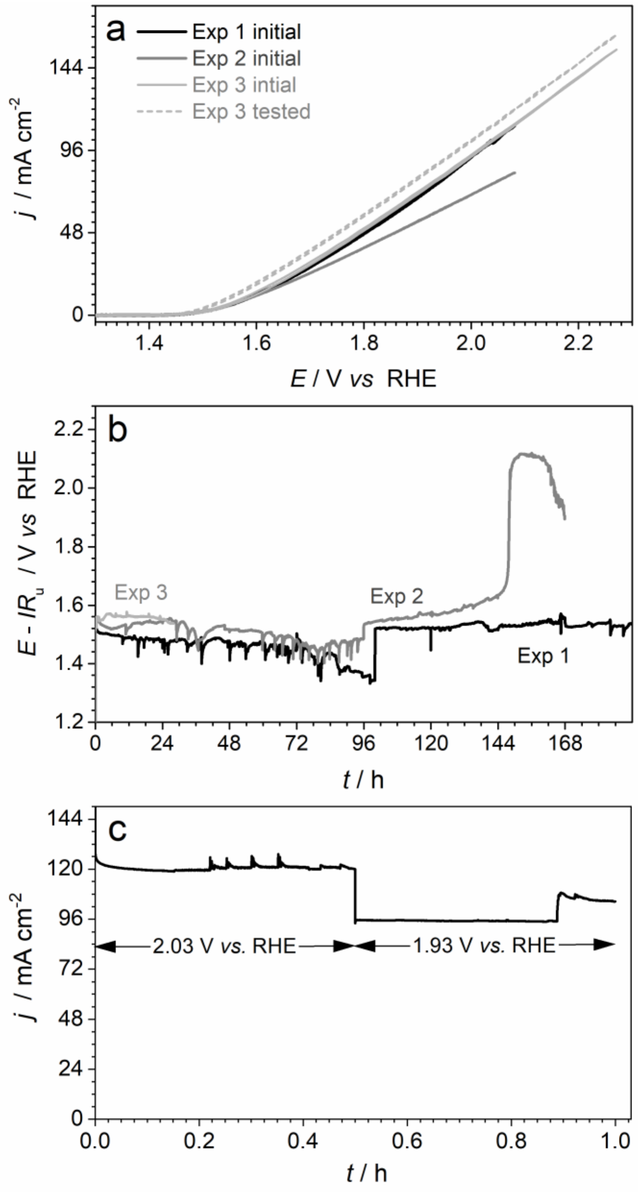

Figure S43. Longer-term performance of [Ru+Sb]O_y in 0.5 M H_2SO_4 at 80 ± 1 °C: (a) initial cyclic voltammetry (v = 0.020 V s^{-1}; potentials are not IR_u-corrected), (b) chronopotentiograms at 10 mA $cm^{-2}_{geom.}$ (data are IR_u-corrected) and (c) subsequently recorded chronoamperograms at 2.03 and 1.93 V *vs.* RHE for experiment 1 (*black*). Currents are normalised to the geometric surface area of the electrodes. Experiment 2 (*grey*) failed after *ca* 100 h of operation due to the irrevocable degradation of the reference electrode. Experiment 3 (*light grey*) included the voltammetric and chronopotentiometric measurements over a shorter period (28 h) only to demonstrate the reproducibility of the catalytic performance.

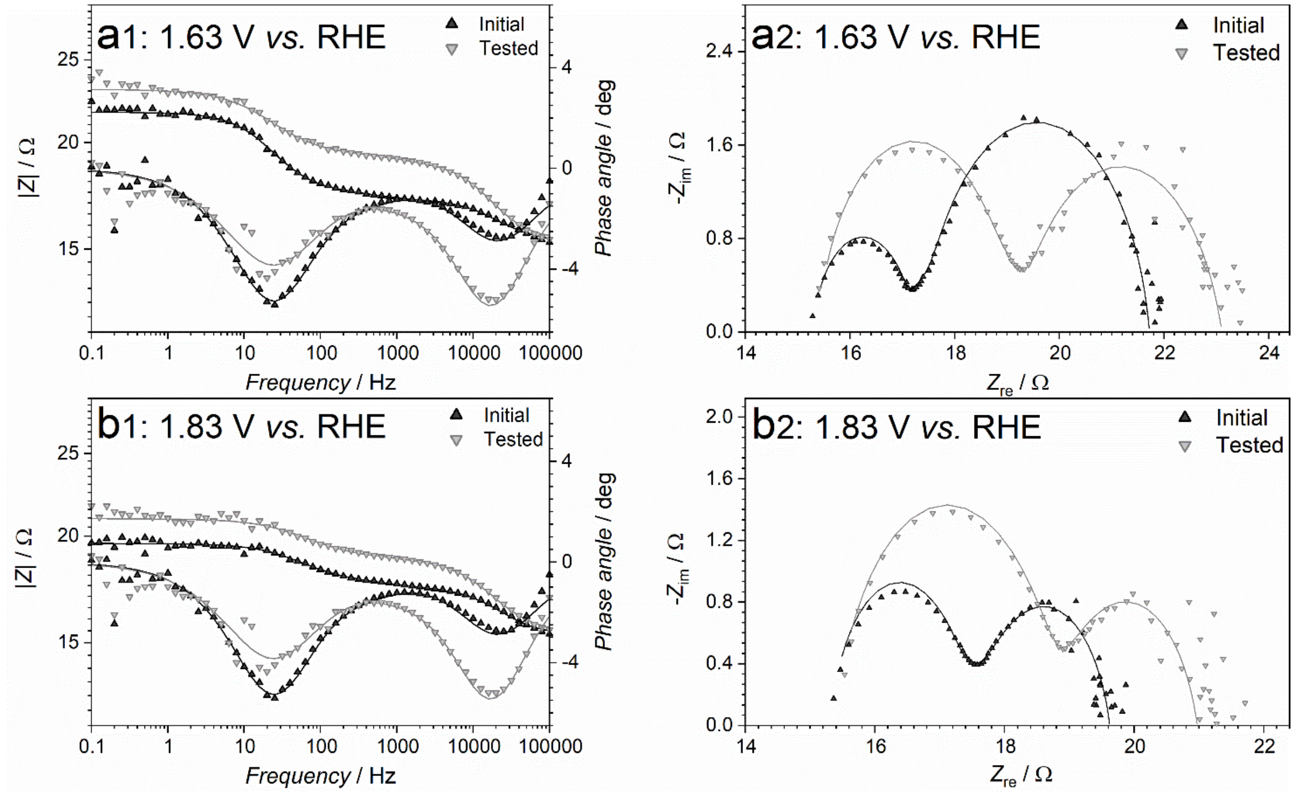

Figure S44. EIS data collected at (a) 1.63 and (b) 1.83 V *vs.* RHE for [Ru+Sb]O_y before (*black*) and after (*grey*) OER tests in stirred 0.5 M H_2SO_4 at 80 ± 1 °C (24 h at 10 mA cm^{-2}; 0.5 h at 1.93 V *vs.* RHE; 0.5 h at 2.03 V *vs.* RHE). Symbols show experimental data, while lines show fits based on the models and parameters summarised in Table S9.

Table S9. EIS fitting parameters for the data in Figure S44 collected for [Ru+Sb]O_y.[a]

E / V *vs.* RHE		R_u / Ω	R_1 / Ω	Q_1 / μF s^{a_1-1}	a_1	R_2 / Ω	Q_2 / μF s^{a_2-1}	a_2	R_{ct} / Ω	Q_{dl} / μF $s^{a_{dl}-1}$	a_{dl}
1.63	initial	15	1.9	14	0.90	0.3	9.5×10^2	1.0	4.3	3.0×10^3	0.89
	tested	15	3.5	6.1	0.94	0.4	5.5×10^2	0.95	3.8	5.1×10^3	0.81
1.83	initial	15	2.0	9.5	0.92	0.4	3.3×10^3	0.75	2.0	4.2×10^3	0.83
	tested	15	3.1	10	0.90	0.5	1.4×10^4	0.52	2.0	4.0×10^3	0.82

[a] Satisfactory fit could be only achieved using R_u[R_1||CPE_1][R_2||CPE_2][R_{ct}||CPE_{dl}] model, where R_u is uncompensated resistance, R_{ct} is charge-transfer resistance of a faradaic process, *viz.* the OER, and CPE_{dl} is a constant phase element representing double-layer capacitance. [R_1||CPE_1] might represent the FTO|catalyst interface, while [R_2||CPE_2] might be associated with the interfaces between grains and/or different phases within the catalyst layer. However, exact nature of these elements is obscure, and no physicochemical significance should be attached to [R_1||CPE_1] and [R_2||CPE_2]. Overall, the presented fitting parameters should be used for semi-quantitative comparisons only.

Table S10. Comparison of the performance of selected thin-film OER catalysts at low pH.

Catalyst	Electrolyte	η_{OER} / V [a]	*j* / mA cm^{-2} [a]	*T* / °C	Stability / h	S number	Ref.
IrO_x	0.05 M H_2SO_4	0.48	10	23	>1		[S12]
Ir	1 M H_2SO_4	0.36	10	23	>2		[S13]
$IrO_x/SrIrO_3$	0.5 M H_2SO_4	0.30	10	23	>30		[S14]
IrO_2	0.5 M H_2SO_4	0.47	10	23	>2		[S14]
IrO_x	1 M H_2SO_4	0.35	10	23	>2		[S15]
RuO_x	1 M H_2SO_4	0.29	10	23	>2		[S15]
Crystalline IrO_2	0.1 M $HClO_4$	0.42	1	23		2×10^7	[S16]
Amorphous IrO_x	0.1 M $HClO_4$	0.29	10	23		9×10^4	[S16]
$SrIrO_3$	0.1 M $HClO_4$	0.38	10	23		9×10^4	[S16]
IrO_x	0.1 M H_2SO_4	0.27	1	23		6×10^4	[S17]
IrO_2/TiO_2	0.1 M $HClO_4$	0.44	1	23		1×10^4	[S18]
$Y_2Ru_2O_7$	0.1 M $HClO_4$	0.32	6.9	23		7×10^4	[S19]
$Bi_2Ru_2O_7$	0.1 M $HClO_4$	0.32	1.8	23		5×10^4	[S19]
$Gd_2Ru_2O_7$	0.1 M $HClO_4$	0.32	3.8	23		5×10^4	[S19]
$Nd_2Ru_2O_7$	0.1 M $HClO_4$	0.32	4.7	23		8×10^3	[S19]
[Ru+Sb]O_y	**0.5 M H_2SO_4**	**0.39 ± 0.03**	**10**	**23**	**> 25**	**2×10^5**	**This work**
		0.34 ± 0.01	**10**		**> 193**	**6×10^5**	
$Ni_xMn_{1-x}Sb_{1.6}O_y$	1 M H_2SO_4	0.67	10	23	≤ 150		[S20]
$CoSb_2O_6$	0.5 M H_2SO_4	0.76	10	23	> 24		[S21]
Fe_2O_3	0.5 M H_2SO_4	0.65	10	23	< 5		[S22]
Co_3O_4	0.5 M H_2SO_4	0.57	10	23	≤ 12		[S23]
[Mn+Sb]O_y	**0.5 M H_2SO_4**	**0.68 ± 0.01**	**10**	**23**	**> 25**	**1×10^4**	**This work**
		0.71	**10**	**80**	**< 96**		

[a] Overpotential of the OER and corresponding current density (per geometric surface area).

SUPPLEMENTARY REFERENCES

S1. Y. Lin, Z. Tian, L. Zhang, J. Ma, Z. Jiang, L. Chen, B. J. Deibert and R. Ge, *Nature Comm.*, 2019, **10**, 162-162.

S2. C. Mun, L. Cantrel and C. Madic, *Nucl. Technol.*, 2006, **156**, 332-346.

S3. I. Povar and O. Spinu, *Journal of Electrochemical Science and Engineering*, 2016, **6**, 145-145.

S4. R. Kötz, H. J. Lewerenz and S. Stucki, *J. Electrochem. Soc.*, 1983, **130**, 825-829.

S5. J. S. Mondschein, J. F. Callejas, C. G. Read, J. Y. C. Chen, C. F. Holder, C. K. Badding and R. E. Schaak, *Chem. Mater.*, 2017, **29**, 950-957.

S6. J. B. Gerken, J. G. McAlpin, J. Y. C. Chen, M. L. Rigsby, W. H. Casey, R. D. Britt and S. S. Stahl, *J. Am. Chem. Soc.*, 2011, **133**, 14431-14442.

S7. M. Chatti, J. L. Gardiner, M. Fournier, B. Johannessen, T. Williams, T. R. Gengenbach, N. Pai, C. Nguyen, D. R. Macfarlane, R. K. Hocking and A. N. Simonov, *Nature Catal.*, 2019, **2**, 457-465.

S8. L. G. Bloor, P. I. Molina, M. D. Symes and L. Cronin, *J. Am. Chem. Soc.*, 2014, **136**, 3304-3311.

S9. V. M. Jansenyl, *Angew. Chem.*, 1978, **90**, 141-142.

S10. J. D. Donaldson, A. Kjekshus, D. G. Nicholson and T. Rakke, *Acta Chemica Scandinavica A*, 1975, **29a**, 803-809.

S11. C.-E. Boman, J. Danielsen, A. Haaland, B. Jerslev, C. E. Schäffer, E. Sunde and N. A. Sørensen, *Journal*, 1970, **24**, 116-122.

S12. Hyung-Suk Oh, Hong Nhan Nong, Tobias Reier, Arno Bergmann, Manuel Gliech, Jorge Ferreira de Araújo, Elena Willinger, Robert Schlögl, Detre Teschner, Peter Strasser, *J. Am. Chem. Soc.* **2016**, 138, 38, 12552−12563.

S13. Charles C. L. McCrory, Suho Jung, Ivonne M. Ferrer, Shawn M. Chatman, Jonas C. Peters, T. F. Jaramillo, *J. Am. Chem. Soc.* **2015**, 137, 13, 4347−4357.

S14. Linsey C. Seitz, Colin F. Dickens, Kazunori Nishio, Yasuyuki Hikita, Joseph Montoya, Andrew Doyle, Charlotte Kirk, Aleksandra Vojvodic, Harold Y. Hwang, Jens K. Norskov, Thomas F. Jaramillo, *Science,* **2016***,* 353, 1011.

S15. Charles C. L. McCrory, Suho Jung, Ivonne M. Ferrer, Shawn M. Chatman, Jonas C. Peters, Thomas F. Jaramillo, *J. Am. Chem. Soc.* **2015**, 137, 13, 4347−4357.

S16. Simon Geiger, Olga Kasian, Marc Ledendecker, Enrico Pizzutilo, Andrea M. Mingers, Wen Tian Fu, Oscar Diaz-Morales, Zhizhong Li, Tobias Oellers, Luc Fruchter, Alfred Ludwig, Karl J. J. Mayrhofer, Marc T. M. Koper, Serhiy Cherevko, *Nat. Catal.* **2018**, 1, 508−515.

S17. Julius Knöppel, Maximilian Möckl, Daniel Escalera-López, Kevin Stojanovski, Markus Bierling, Thomas Böhm, Simon Thiele, Matthias Rzepka, Serhiy Cherevko, *Nat Commun.* **2021**, 12, 2231.

S18. Chuyen Van Pham, Melanie Bühler, Julius Knöppel, Markus Bierling, Dominik Seeberger, Daniel Escalera-López, Karl J.J. Mayrhofer, Serhiy Cherevko, Simon Thiele, Applied Catalysis B: Environmental, **2020**, 269, 118762.

S19. McKenzie A. Hubert, Anjli M. Patel, Alessandro Gallo, Yunzhi Liu, Eduardo Valle, Micha Ben-Naim, Joel Sanchez, Dimosthenis Sokaras, Robert Sinclair, Jens K. Nørskov, Laurie A. King, Michal Bajdich, and Thomas F. Jaramillo, *ACS Catal.* **2020,** 10, 12182−12196.

S20. I. A. Moreno-Hernandez, C. A. Macfarland, C. G. Read, K. M. Papadantonakis, B. S. Brunschwig, N. S. Lewis, *Energy Environ. Sci.* **2017**, *10*, 2103.

S21. T. A. Evans, K. S. Choi, *ACS Appl. Energy Mater.* **2020**, *3*, 5563−5571.

S22. W. L. Kwong, C. C. Lee, A. Shchukarev, E. Björn, J. Messinger, *J. Catal.* **2018**, *365*, 29.

S23. J. S. Mondschein, J. F. Callejas, C. G. Read, J. Y. C. Chen, C. F. Holder, C. K. Badding, R. E. Schaak, *Chem. Mater.* **2017**, *29*, 950.